RRS JAMES COOK Barter Cruise

IODP-Presite survey for "The MoHole": Seismic structure of fast spreading lithosphere and hydrothermal circulation, Guatemala Basin

Cruise No. JC228

Leg1: 03.12.2022 – 09.01.2023
Caldera (Costa Rica) – Caldera (Costa Rica)

Leg2: 13.01.2023 – 22.01.2023
Caldera (Costa Rica) – Caldera (Costa Rica)
GUATOPS

Ingo Grevemeyer, Timothy Henstock & Ingo Klaucke

Ingo Grevemeyer
GEOMAR Helmholtz Centre for Ocean Research Kiel

2023

Table of Contents

1 Cruise Summary

1.1 Summary in English

The formation, evolution, subduction, and recycling of oceanic lithosphere is a fundamental tenet of plate tectonics. This cycle is the primary mechanism for thermal and chemical exchanges between the solid Earth and the hydrosphere. In collaboration a German-UK consortium conducted an integrated geophysical and geological study during the barter cruise JC228 aboard the British RRS JAMES COOK, sampling fast-spreading ocean lithosphere of the northern Cocos Plate from its formation to subduction in the Mid-America Trench. We collected seismic reflection (MCS) and refraction (WAS) data along a linear transect with grids in three focus areas; two were on the passively cooling oceanic plate, the third spanned the transition into the subduction zone. There, faults that form as the plate bends allow seawater to penetrate through the crust and into the upper mantle and thereby hydrate mantle just before it subducts. Fluid flow associated with these plate bending faults were investigated using geophysical and pore water data, including high-resolution bathymetry, heat flow and coring. The cruise JC228 is going to deliver key information on the evolution of oceanic lithosphere as well as provide essential site survey information for two IODP Proposals: the flagship MoHole to Mantle initiative (M2M; IODP-805MDP) and the Bend Fault Serpentinization experiment (approved IODP-876Pre).

1.2 Zusammenfassung

Die Plattentektonik beschreibt die Bildung, Entwicklung, und das Recycling der Ozeanischen Lithosphäre in den Subduktionszonen als einen Kreislauf. Dieser Kreislauf ist fundamental für den Wärme- und Stoffaustausch zwischen der Geo- und der Hydrosphäre. Im Rahmen einer Deutsch-Britischen Kooperation wurde auf der Expedition JC228 des Britischen Forschungsschiffs RRS JAMES COOK schnell-spreizende Kruste und Lithosphäre der Cocos Platte sowie ihre Variabilität von der Spreizungsachse bis in den Tiefseegraben von Mittelamerika charakterisiert. Im Mittelpunkt der Arbeiten standen Mehrkanalreflexionsseismische (MCS) sowie refraktions- und weitwinkelseismische (WAS) Messungen entlang eines Korridors sowie in drei Regionen, wo wir detaillierte Studien zur lateralen Variabilität der Kruste durchgeführt haben. Zwei dieser Arbeitsgebiete charakterisieren normale Ozeanische Kruste während im dritten Gebiet der Übergang in den Tiefseegraben und die Einflussnahme der dort auftretenden Verwerfungen auf die Struktur, physikalischen Eigenschaften und Hydrogeologie untersucht wurden. Hier stand vor allem die die Hydrierung des Erdmantels im Mittelpunkt. Die Expedition fand im Kontext von zwei geplanten Bohrprojekten statt und akquirierte die notwendigen Voruntersuchungen für das im IODP Forschungsplan vorgesehene „MoHole“ (M2M; IODP-805MDP) sowie für einen Bohrvorschlag zur Untersuchung der Mantelhydrierung (IODP-876Pre) in Tiefseegräben.

2 Participants

2.1 Principal Investigators

Name	Institution
Grevemeyer, Ingo, Prof	GEOMAR
Henstock, Timothy J., Prof	U. Southampton & NOC
Teagle, Damon A.H., Prof	U. Southampton & NOC
Morgan, Jason P., Prof (formerly Royal Holloway UK)	SUTECH, China
Vannucchi, Paola, Prof (formerly Royal Holloway UK)	U. Florence
Kaul, Norbert, Dr	University of Bremen

2.2.1 Scientific Party Leg 1

Name	Discipline	Institution
Grevemeyer, Ingo, Prof	Refraction seismology / Chief Scientist	GEOMAR
Henstock, Tim, Prof	Marine seismics / Co-Chief Scientist	U. Southampton
Dannowski, Anke, Dr	Refraction seismology / OBS	GEOMAR
Marjanovic, Milena, Dr	Marine seismics	IPGP
Hilbert, Helene-Sophie	OBS	GEOMAR
Pitcairn, Ben	OBS	Durham/OBIC
Gonzalez-Nakazawa, Alex	OBS technician	Durham/OBIC
Gutierrez-Nuno, Rafael	OBS technician	NOC/OBIC
Bauer, Benedikt	OBS, watchkeeper, student	GEOMAR
Panachi, Esther	OBS, watchkeeper, student	GEOMAR
Ritter, Josefa	OBS, watchkeeper, student	GEOMAR
Li, Lianjun	MMO, watchkeeper	Imperial
Lai, Szu-Ying	MMO, watchkeeper	U. Southampton
Viera-Rivero, Josue	SSS Tech, streamer, gravity, magnetics	NOC
Pedder, Joshua	SSS Tech, streamer, gravity, magnetics	NOC
Leadbeater, Andrew	NMF Tech, airguns, streamer	NOC
Cheeseman, Dean	NMF Tech, airguns, streamer	NOC
Arnott, Jack	NMF Tech, airguns, streamer	NOC
Weeks, Martin	NMF Tech, airguns, streamer	NOC
Phipps, Richard	NMF Tech, airguns, streamer	NOC
Richardson, Will	NMF Tech, airguns, streamer	NOC
Mayer, John	Streamer data acquisition	NOC/contractor
Dar, Marvin	Streamer data acquisition	NOC/contractor

2.2.2 Scientific Party Leg 2

Name	Discipline	Institution
Klaucke, Ingo, Dr	Mapping, bathymetry / Chief Scientist	GEOMAR
Henstock, Tim, Prof	Bathymetry / Co-Chief Scientist	U. Southampton
Vannucchi, Paola, Prof	Structural geology	U. Florence
Marjanovic, Milena, Dr	Seismic interpretation	IPGP
Kaul, Norbert, Dr	Heat flow	U. Bremen
Cooper, Matthew, Dr	Pore water chemistry	U. Southampton
Bodenmann, Adrian	AUV data analyses	U. Southampton
Hilbert, Helene-Sophie	Bathymetry	GEOMAR
Bauer, Benedikt	Watchkeeper, student	GEOMAR
Panachi, Esther	Watchkeeper, student	GEOMAR
Ritter, Josefa	Watchkeeper, student	GEOMAR
Li, Lianjun	MMO, watchkeeper	Imperial
Ploetz, Aline	Heat flow	U. Bremen
Schmidt, Jan-Niklas	Heat flow, student	U. Bremen
Pedder, Joshua	SSS Tech, gravity, magnetics	NOC
Roper, Daniel	NMF Tech, AUV	NOC
Shepherd, Owain	NMF Tech, AUV	NOC
Fairbairn, Stewart	NMF Tech, AUV	NOC
Phillips, Alexander	NMF Tech, AUV	NOC
Morris, Ashley	NMF Tech, AUV	NOC
Leadbeater, Andrew	NMF Tech, coring, hardware	NOC
Arnott, Jack	NMF Tech, coring, hardware	NOC
Weeks, Martin	NMF Tech, coring, hardware	NOC
Phipps, Richard	NMF Tech, coring, hardware	NOC
Richardson, Will	NMF Tech, coring, hardware	NOC
Fallas, Carolina	Observer	U. San Jose

2.3 Participating Institutions

GEOMAR	Helmholtz-Zentrum für Ozeanforschung Kiel, Germany
U. Southampton	University of Southampton, UK & NOC
U. Durham / OBIC	University of Durham & Ocean-Bottom-Instrument Consortium, UK
NOC	National Oceanographic Centre, Southampton, UK
Imperial	Imperial College, London, UK
IPGP	Institut de Physique du Globe de Paris, France
U. Florence	University of Florence, Italy
U. Bremen	Dept. Geosciences, University of Bremen, Germany
U. San Jose	University of San Jose, Costa Rica

3 Research Program

3.1 Description of the Work Area

"*Perhaps it is true that we won't find out as much about the Earth's interior from one hole as we hope. To those who raise that objection I say, if there is not a first hole, there cannot be a second or a tenth or a hundredth hole. We must make a beginning.*" (Harry Hess, April 1958)

3.1.1 Background – Oceanic crust and its base the seismic Moho

Almost 70% of Earth's surface are covered by water. However, a number of marginal seas, like the North Sea and Baltic Sea among others, are floored by continental crust, leaving 57-60% of the Earth's surface being formed by seafloor spreading along the global mid-ocean spreading ridge (MOR) system. Consequently, oceanic lithosphere created over the last 180 Myrs at the MOR system is by far the largest geological unit on our planet.

The oceanic crust, forming the upper portion of the lithosphere, is formed by melting of a pyrolite mantle at the mid-ocean ridges, extracting basaltic liquids to form the ocean crust and leaving a residue of harzburgite forming the underlying mantle. About two-thirds of the magma cools and crystallizes in the lower portion of the ocean crust. The remaining magma is extruded at the seabed or forms the sheeted-dykes of the upper crust. Extruded basalts and sheeted-dykes form the so called basaltic layer 2; the lower crust or layer 3 is composed of gabbroic rocks. This layered structure of the oceanic crust was initially derived from seismic refraction measurements. The first classic compilation of seismic data of Raitt (1963) and its layered structure formed the reference for seismic profiles and the geologic structure of the crust for the last decades. The upper igneous crust or layer 2 is a region of strong velocity gradients, while the lower crust or layer 3 is relatively homogeneous, although it does show an increase in velocity with depth (e.g., Whitmarsh, 1978). Further, the upper crust has been sub-divided the in layer 2A, composed of extruded basalts, and layer 2B, formed by basaltic sheeted dikes. The lower crustal layer 3 is also called the "oceanic layer" (e.g., White et al., 1992). As crust ages, sediments accumulate blanketing the igneous basement, creating layer 1.

Seismic, bathymetric, and marine geological observations indicate that oceanic crust formed at fast spreading rates (full rate >80 mm yr^{-1}) is much less variable than crust formed at slow spreading rates (<40 mm yr^{-1}) (e.g., White et al., 1992) and is closer to an ideal model of oceanic crust, called the Penrose model. The Penrose model was derived from ophiolites and hence fragments of oceanic crust and upper mantle that have been uplifted and emplaced on continental margins or in accretionary prisms and island arcs. According to the 1972 Geological Society of America (GSA) Penrose Conference, an idealized, complete ophiolite contains, from the base upward, mantle peridotites, layered ultramafic rocks and gabbros, isotropic gabbros, a sheeted dike complex, and an extrusive sequence, composed of pillow basalts and massive flows, overlain by radiolarian chert and/or pelagic limestone (e.g., Dilek, 2003). Originally, ophiolites were interpreted to have developed mainly at ancient mid-ocean ridges. However, more recent geochemical studies of ophiolites challenged this view and suggested the association of magma evolution with subduction zones. This paradigm shift in the evolving ophiolite concept led to the definition of supra-subduction zone ophiolites (e.g., Dilek, 2003). Thus, the Penrose model may represent oceanic crust formed in a back-arc spreading system rather than crust formed at a “normal” mid-ocean ridge, challenging a concept being recited in numerous text books.

Gaining a better understanding requires new data from the largest geological formation of our planet. Oceanic crust created at fast-spreading ridges appears to be uniformly layered and relatively homogeneous, reflecting a relatively uniform mode of accretion. Further, although <20% of modern ridges are moving apart at fast spreading rates, nearly 50% of present-day oceanic crust and ~30% of the Earth’s surface have been produced by fast spreading (e.g., Müller et al., 2008), suggestion that fast-spreading crust should be the target for future detailed geological sampling.

Current understanding of the deep structure and composition of oceanic crust is derived from seismic studies or from geological surveys of settings where deep crustal rocks have been exposed at the seafloor by faults, like the Hess deep. Although limited, the structure of the oceanic crust has been increasingly influenced by data and samples from a relatively small number of bore holes, collected during the Deep Sea Drilling Project (DSDP), the Ocean Drilling Program (ODP) and the Integrated Ocean Drilling Program (IODP). However, only the ODP/IODP multi-leg campaign at Site 1256 in the Guatemala Basin provides a continuous in situ section of fast spreading oceanic crust from the extrusive lavas, through the sheeted dikes and down into the uppermost gabbros (e.g., Teagle et al., 2012). Thus, major part of the lower crust was never sampled and not a single drill hole penetrated the crust mantle boundary, called the Moho (after the Croatian seismologist Mohorovičić, who found that crust and mantle are separated by a discontinuity, called the Mohorovičić discontinuity or short Moho).

The goal of drilling a complete section through the oceanic crust and into the upper mantle (Fig. 3.1) has been reiterated throughout the history of scientific ocean drilling. This fact is highlighted in the IODP Initial Science Plan. Today, the "21st Century MoHole" Initiative is one of eight high-priority scientific objectives of the new IODP. It is interesting to note that the idea of drilling the Moho marked the beginning of marine scientific drilling, issuing the “Project MoHole” in the 1950s, which was an attempt to retrieve a sample of material from the Earth's mantle by drilling a hole through the entire Earth's crust, through the Mohorovičić discontinuity, and into the Earth’s mantle. The project was suggested in 1957 by Walter Munk and other members of the American Miscellaneous Society (including the famous marine geologists Harry Hess and Roger Revelle) with funding from the National Science Foundation (NSF). In 1961, the oil drillship CUSS I drilled 183 m into the seafloor, including 13 m of basaltic basement. Unfortunately, the project was abandoned, but scientific offshore drilling went ahead, issuing the DSDP, ODP, and IODP. Today, however, new technologies

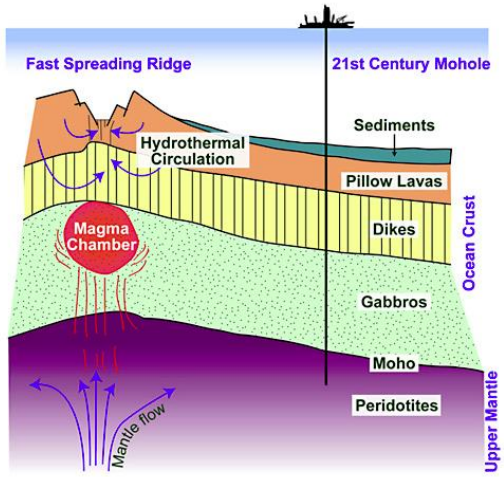

Fig. 3.1 MoHole, drill the entire oceanic crust from top to bottom.

and advances in our understanding of the oceanic lithosphere suggest that drilling Moho is still a challenge, but feasible (e.g., Teagle and Ildefonse, 2011).

Sampling a complete section of fast spreading crust would address a number of fundamental questions, including (Ildefonse et al., 2010; Teagle and Ildefonse, 2011):

- What physical properties cause the Mohorovičić discontinuity, and what is the geological nature of this boundary zone?
- How is the oceanic crust formed at the mid-ocean ridges, and what processes influence its subsequent evolution? What are the geophysical signatures of these magmatic, tectonic, hydrothermal, biogeochemical, and chemical processes?
- What can we infer about the bulk composition of the oceanic crust, and what are the magnitudes of interactions with the oceans and biology and their influence on global chemical cycles?
- What are the limits of life, and the factors controlling these limits? How do the biological community compositions change with depth and the evolving physical and chemical environments through the oceanic crust?
- What is the physical and chemical nature of the uppermost mantle, and how does it relate to the overlying magmatic crust?

Drilling a complete section of the oceanic crust is a major challenge and costly. Thus, scientist defined in numerous meetings and workshops criteria any potential MoHole site should satisfy (Ildefonse et al., 2010), defining the best possible site:

a) Crust formed at fast-spreading rate (>40 mm yr^{-1} half rate).

b) Simple tectonic setting with very low-relief seafloor and smooth basement relief; away from fracture zones, propagator pseudo-faults, relict overlapping spreading basins, seamounts, or other indicators of late-stage intraplate volcanism. Connection to the host plate active constructive and destructive boundaries would provide important scientific information.

c) Crustal seismic velocity structure should not be anomalous relative to current understanding of "normal" fast-spreading Pacific crust, indicative of layered structure.

d) A sharp, strong, single-reflection Moho imaged with Multi-Channel Seismic (MCS) techniques.

e) A strong wide-angle Moho reflection (PmP), as observed in seismic refraction data, with distinct and clearly identifiable sub-Moho refractions (Pn).

f) A clear upper mantle seismic anisotropy.

g) A crust formed at an original latitude greater than ±15°.

h) A location with relatively high upper crustal seismic velocities indicative of massive volcanic formations to enable the initiation of a deep drill hole.

Satisfying requirements for points a–e is essential for success. More flexibility is allowed in meeting points f–h, which are highly desirable but not essential.

Three potential MoHole areas were defined for the Pacific Ocean (Ildefonse et al., 2010; Teagle and Ildefonse, 2011), including the outer bulge of the Hawaiian flexural swell, the area off Baja California near the original "Project MoHole" site, and the Guatemala basin where ODP/IODP site 1256D penetrated 1500 m into the oceanic crust. However, lithosphere farther east of site 1256 will be older than 15 Myrs and hence would support a lower thermal gradient and consequently lower temperatures when drilling into the Moho.

Defining a MoHole site requires a number of seismic pre-site survey data (see criteria above). In a British-German co-funded pre-site survey the cruise JC228 is going to support the flagship IODP MoHole to Mantle initiative (M2M; IODP-805MDP), surveying potential MoHole sites in the Guatemala Basin. In addition, we know that oceanic lithosphere is being modified by bending-related faulting in the trench-outer rise, facilitating migration of water into the upper mantle, causing hydration and hence serpentinization. To the east of the potential M2M sites, bending-related faulting is most prominent and was well-studied in the German Centre of Excellence SFB574 (e.g., Grevemeyer et al., 2005; 2007; Ivandic et al., 2008). For this area the new Bend Fault Serpentinization experiment (IODP-876Pre submitted Oct 2014) has been proposed. Thus, the cruise JC228 will deliver key information on the evolution of oceanic lithosphere as well as provide essential site survey information for two IODP proposals.

A new reference for the oceanic crust using wide-angle data

Since 1950s when Maurice Ewing from Lamont-Doherty Earth and his colleagues started exploration the oceans and the crust forming the seabed, a wealth of data was obtained, still shaping our views on the oceanic crust and lithosphere. The primary source of our knowledge of the structure of oceanic crust is on the interpretation of seismic refraction experiments. One of the most striking results from seismic refraction experiments was that oceanic crust has a nearly uniform thickness compared with the continental crust. The two most cited global compilations of data showed that oceanic crust is 6.57 ± 1.61 km (Raitt, 1963) or 7.08 ± 0.78 km (White et al., 1992) thick. However, the large standard deviations suggest that it is difficult to interpret the results of statistical studies in terms of structural variability. Further, it is important to note that crustal thickness estimates depend on the remote sensing technique used to explore the thickness of the crust and on the interpretation method. Thus, some of the variability seen in compilations depend on the inversion or modelling approach. For example, Raitt (1963) compiled crustal thickness estimates based on slope-intercept times and hence layers with constant velocity, while White et al. (1992) compiled data based on 1-D modelling of synthetic seismograms, where a crust/mantle transition zone is introduced. Consequently, the exact depth of the Moho has been more challenging to define, for Moho is considered a transition zone rather than an abrupt boundary. White et al. (1992) noted that the use of synthetics seismogram methods caused an increase of typically 20% over the thickness calculated by the slope-intercept method.

All these compilations are over 30 years old and depend on sonobuoy data or on sparse numbers of ocean-bottom-seismometers (OBS) place along seismic lines collected in the 1970s and 1980s. Since the 1990s, the number of available OBS has increased and modern surveys use repeating airgun sources and instrument spacings of 5 to 10 km, allowing detailed 2-D interpretation and inversion of data. Further, crustal thickness estimates are not just defined using first arriving seismic refraction branches (as in the slope-intercept method), but can be supported by wide-angle reflection from the crust-mantle boundary, the so called

PmP, placing much more robust constraints on crustal thickness. Further, in modern joint reflection and refraction tomography (e.g., Korenaga et al., 2000) of densely spaced OBS data both first arrivals and later arriving reflections contribute to derived high-resolution crustal velocity models that can be used to yield precise crustal thickness estimates and processes from seismic velocity models.

The oceanic lithosphere is formed by seafloor spreading and hence melting of mantle, which in turn, affects the velocity structure of the oceanic crust. The amount of melt produced by adiabatic decompression of the mantle and the composition of the resultant igneous crust depend on the temperature, composition, and water content of the mantle source (e.g., Korenaga et al., 2002). Normal oceanic crust with a thickness of 6-7 km and Mid-Ocean Ridge Basalt (MORB) like composition is the result of decompression melting of a mantle source composed of dry pyrolite with a mantle temperature of ~1300°C (McKenzie and Bickle, 1988). Thus, crustal formation occurs as a passive response to seafloor spreading (i.e., passive upwelling). Higher mantle temperatures or compositional anomalies may cause buoyant upwelling of the mantle (i.e. active upwelling). The combination of active upwelling and higher mantle temperatures, or the presence of a more fertile mantle source, will produce larger amounts of melting and, likely, a thicker crust. Crustal thickness and lower crustal velocity have been used as proxies for mapping the effects of mantle melting on crustal accretion (e.g., Korenaga et al., 2002).

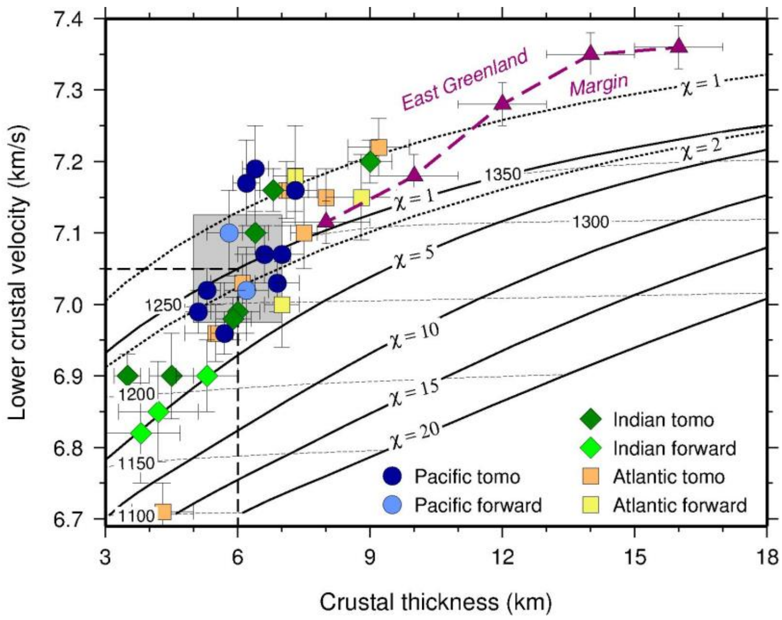

Fig. 3.2 Melt regime during seafloor spreading: theoretical crustal thickness versus seismic velocity of primary melts generated by the model of Korenaga et al. (2002): Note, normal fast spreading crust (dark blue symbols) provide ~6 km of crust and lower crustal velocity of 7-7.1 km/s; data compiled by and figure from Grevemeyer et a. (2018).

Korenaga et al. (2002) provided a steady state mantle melting model that could be used to investigate the relationship between mantle temperature, upwelling, and mantle composition on one hand and lower crustal seismic velocity and crustal thickness on the other hand (Fig. 3.2). A set of parameters is needed to define a reference model. Crustal thickness and lower crustal velocity are calculated for mantle potential temperatures varying from 1100°C to 1350°C, and an upwelling ratio at the base of the damp melting zone, χ, varying from 1 to 20. It is interesting to note that the seismic structure of crust generated at the East Pacific Rise, i.e. that of “normal” oceanic crust (e.g., Grevemeyer et al., 1998; Canales et al., 1998), is consistent with that expected for a crust generated by passive decompression melting of dry pyrolitic mantle (χ ~1) with a potential temperature of 1250–1300°C, supporting that crust formed along fast-spreading ridge represents lithosphere generated by simply melting processes. Oceanic crust that deviates from this simple structure may indicate variations in melting or mantle temperature.

Grevemeyer et al. (2018) used this process orientated assessment to provide new bounds on the velocity structure and crustal thickness of normal crust. Thus, compiling velocity profiles from seismic tomography of crust that formed by normal mantle temperatures of 1100°C to 1350°C and passive upwelling, resulted in a well-defined reference crust (Fig. 3.3). The new assessment incudes data from a number of different surveys, summarizing in total more than 100 OBS/H stations from both the Indian Ocean and the Pacific Ocean. The most striking features is a nearly constant Lower crustal velocity of 6.9-7 km/s and a crustal thickness of 6 ± 1 km. It is this structure any site chosen for the MoHole should have.

In addition to the rather homogeneous thickness of oceanic crust, one of the most striking features emerging from seismic studies is the variability of layer 2. Early interpretations by Raitt (1963) demonstrated that layer 2 compressional wave velocities range widely, from less than 3.0 km/s to more than 6.0 km/s. Since laboratory measurements on fresh basalts yield velocities of about 6 km/s, low seafloor velocities can only be explained by abundant porosity at a scale larger than that sampled by drilling or dredging (e.g., Hyndman and Drury, 1976).

Seismic experiments near spreading ridges indicated that seismic velocities in the top of the igneous crust (i.e., layer 2A) are typically much lower than those in mature oceanic crust. It has been established that the velocity increase is related to hydrothermal precipitation of secondary minerals in open pore spaces of the extrusive basaltic crust. As a consequence, rocks become chemically altered with increasing water/rock ratio and hence crustal age. In the Pacific, seismic velocity at the top of juvenile crust is >2.5 km/s. With distance from the ridge axis and hence age velocities increased rapidly increased close to the ridge axis (~0.8-1 km/s per 1 Myrs) and slowly thereafter (0.1-0.2 km/s per 1 Myrs),

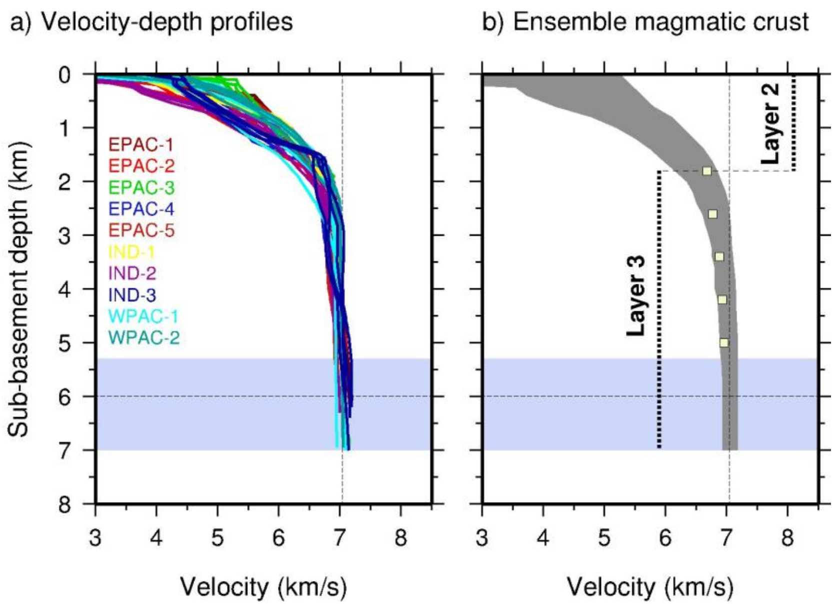

Fig. 3.3 Crustal structure from all surveys plotting within the grey field of Fig. 2.2, providing a new reference base for normal oceanic crust based on joint refraction and reflection tomography, providing much tighter error bounds on the lower crustal velocity structure and crustal thickness when compared to older compilations (e.g., White et al., 1992); from Grevemeyer et a. (2018).

reaching a velocity of ~4.5 km/s in 10 Myrs old crust (e.g., Grevemeyer et al., 1999), closely matching trends derived from global data sets (e.g., Grevemeyer and Bartetzko, 2003). Further, seismic velocities exceeding 4.5 km/s in the uppermost basement were recognized being an important feature of mature crust and is used to define "drillable" basement in pre-site surveys. While seismic velocity in the upper crust indicated a time-depending and hence evolutionary process are velocities at mid- and lower crustal levels rather un-changed, providing little indications that hydrothermal flow or alteration affects the lower crust when lithosphere moved away from the ridge crest.

Structure of the oceanic crust from multi-channel seismic (MCS) data

In the early days of marine exploration, seismic reflection surveys with single hydrophones or short hydrophone arrays just allowed to study layer 1 and hence the sediment blanketing the oceanic basement. However, over the years modern seismic airgun arrays and long hydrophone arrays or streamers provided images of the entire oceanic crust, including seismic Moho (e.g., Reston et al., 1999; Kodaira et al., 2014). In general, images of slow spreading crust indicated features supporting tectonism and hence large lateral variations in the style of faulting and reflectivity pattern, while fast spreading crust indicated similar feature in different parts of the Pacific Basin, supporting homogeneous reflectivity pattern and clear Moho reflections.

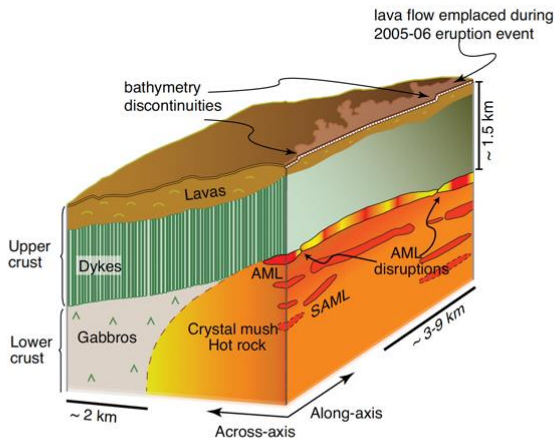

Fig. 3.4.: Data-based illustration of oceanic crust formed at the East Pacific Rise 9º50'N (Marjanović et al., 2015). Color variation from red to yellow within the AML represents low to high crystalline component variation, respectively (Fig. not to scale).

Fast spreading crust shows different features for ridge crests when compared to mature crust. Along the ridge crest a continuous inverse polarity reflector indicates the presence of melt and axial magma lens (AML) about 1-1.5 km below seafloor (e.g., Detrick et al., 1987; Marjanović et al., 2015). In addition, the upper crust indicates a wide-angle signal 200-700 m below the seafloor, being interpreted as the base of the extrusive lava pile, called the base of layer 2A (e.g., Detrick et al., 1987; Marjanović et al., 2018). Further, a reflection of the crust-mantle boundary is often found in seismic profiles crossing the ridge crest, called the seismic Moho. Overall, crust remains rather transparent, but where seismic Moho is detected, it shows some variability in thickness and the appearance of Moho (e.g., Barth and Mutter, 1996; Aghaei et al., 2014).

Moving away from the ridge crest, the layer 2A reflector generally disappears, being associated with increasing velocities in the upper crust as described above. In some setting an upper crust reflector occurs that might be associated with the layer 2/layer 3 transition zone (Reston et al., 1999; Kodaira et al., 2014). The most prominent feature of fast-spreading mature crust is the Moho-reflector and short dipping reflectors, dipping towards the spreading axis and terminating at the Moho (Reston et al., 1999; Kodaira et al., 2014). These reflectors are interpreted being related to shearing caused by active upwelling and mantle flow. Any MoHole site should be characterized by a clear, well-defined and continuous Moho reflection.

Hydrothermal cooling and heat flow

At mid-ocean ridges, the lithosphere is formed continuously by seafloor spreading. As lithosphere spreads away from the ridge axis it cools and subsides. Following the realization that seafloor heat flow is highest at the ridge crest and decreases with distance and hence plate age (Langseth et al., 1965) the systematic variation of ocean depth and heat flow with age became the primary constraint on models of the thermal evolution of the lithosphere (e.g., Stein and Stein, 1992;). However, a significant discrepancy exists between the heat flow measured at the seabed and the higher values predicted by thermal models of a conductively cooling lithosphere. This heat flow discrepancy is thought to reflect the transport of significant amounts of heat by circulating fluids (Lister, 1972). Results of this circulation are exhibited most spectacularly at the ridge crests where venting of fluids at temperatures up to 400°C occurs. On the ridge flanks the ongoing heat loss of the lithosphere drives the circulation of fluids through the porous upper layers of crust. Here at the much lower temperatures the vigor of hydrothermal circulation is reduced. However, due to the vast areas of the seafloor where such circulation can occur, perhaps 70% of the hydrothermal heat loss is off axis (Stein and Stein, 1994).

In the axial zone, the observation of high temperature fluid venting from open fissures is evidence that high permeability pathways like fault zones control convective fluid circulation and hence the cooling process of very young crust. Within older crust, fluid circulation continues and appears to be controlled by the background permeability,

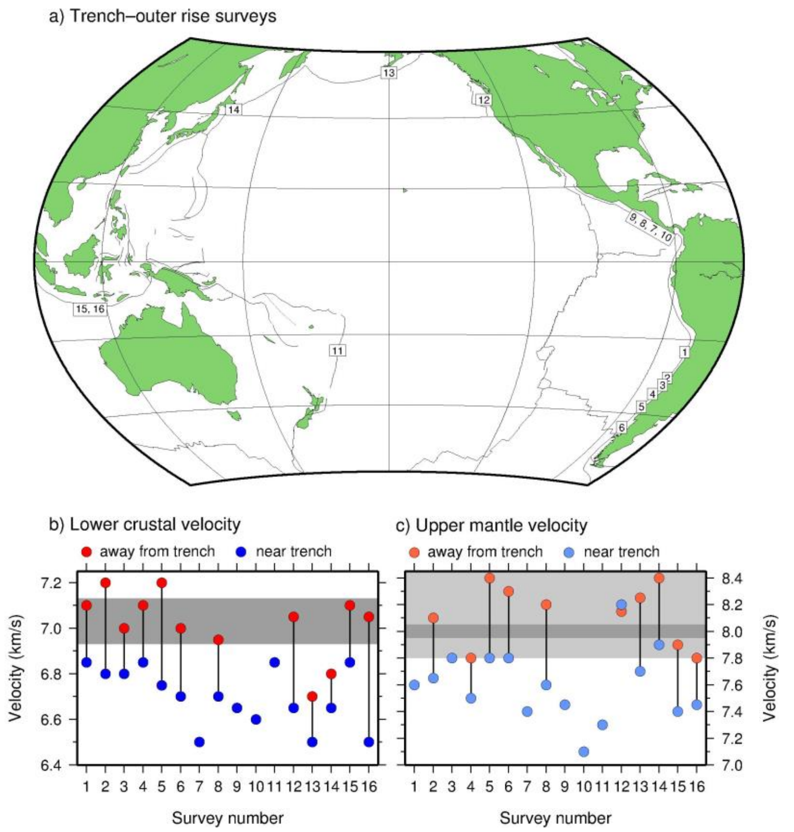

Fig. 3.5 Compilation of results from seismic profiles approaching deep-sea trenches; a) mantle velocity, and b) lower crustal velocity. Note, velocity reduction in the vicinity of the trench is a global phenomenon, indicating alteration and hydration; redrawn from Grevemeyer et a. (2018).

yielding a heat flow pattern which roughly mimics the topography (e.g., Davis and Villinger, 1992; Fisher et al., 1994). In general, heat flow determinations on the ridge flanks reveal values well below the theoretical prediction (Stein and Stein, 1994; Villinger et al., 2002), suggesting that hydrothermal circulation is vigorously removing heat out of the oceanic lithosphere. Most importantly, seamounts are critical in affecting and controlling the hydrogeological system on the flank of MOR (e.g., Villinger et al., 2002; Hutnak et al., 2008).

In crust approximately older than 60 Ma, however, the observed heat flow approaches the predicted heat flow derived from plate cooling models, indicating that hydrothermal circulation has largely ceased (Stein and Stein, 1994). The seafloor age where the observed heat flow approaches the predicted heat flow is often called the 'sealing age'. The sealing age is controlled either by a sediment cover with low vertical permeability, restricting the exchange of seawater between the crust and ocean, or precipitation of secondary minerals, reducing the permeability of the crust to values too low to support hydrothermal circulation. Thus, the sealing age is strongly dependent of regional features, like seafloor relief and sedimentation rate, varying from a few millions of years to ~80 Ma. (e.g., Villinger et al., 2002; Stein and Stein, 1994).

Bending-related faults in the trench-outer rise

Bound H_2O stored within the oceanic lithosphere is associated with hydrothermal alteration. In general, hydrothermal activity decreases as the lithosphere moves away from a mid-ocean ridge, because the uppermost crust is sealed by precipitation of secondary alteration products and sediments deposited on top of the crust restrict the flow of seawater into the igneous basement. However, in the trench-outer rise area, where the subducting lithosphere bends into the trench, faulting associated with bending and large earthquakes re-activates old faults and/or creates new faults, cutting into the uppermost mantle (e.g., Grevemeyer et al., 2005). At sediment starved trenches, bending-related faults may breach the sedimentary cover to allow recharge and discharge of seawater; seawater migrating down to mantle depth may cause serpentinization.

Seismic data have been shown to be a useful technique to yield the state of hydration of the incoming subducting plate, showing that seismic P-wave velocity systematically decreases world-wide trench-wards both in the lower crust and the upper mantle (Fig. 3.5) highlighting an evolutionary process of global importance (e.g., Grevemeyer et al., 2018). Thus, seismic compressional wave velocity decreases during serpentinization, from nearly ~8.0-8.2 k/s in non serpentinized peridotites, to ~4.5 km/s at 100% transformation of peridotite to serpentinite. At a number of trenches, including Nicaragua, Chile, and Tonga, it has been revealed that bending-related faulting is indeed an evolutionary process (e.g., Grevemeyer et a., 2007; Ivandic et al., 2008; Contreras-Reyes et al., 2008; 2010), facilitating hydration prior to subduction. Seismic data suggest that trench-outer rise hydration creates a reservoir of chemically bound water in the uppermost mantle that is roughly in the same order as crustal hydration caused at the mid-ocean ridge. For example, offshore of southern Nicaragua a velocity reduction of 0.2-0.5 km/s and hence velocities of 7.6-7.8 km/s were observed within the uppermost 5 to 10 km of the mantle (e.g., Ivandic et al., 2008). Moving further north where bending-related faulting is much more profound velocity was even further reduced to values of 7.3-7.5 km/s. In the first case values suggest a degree of serpentinization in the order of 12 to 17%. In the second case serpentinization reached 19 to 24%, corresponding to a water content of ~2.5-3.1 wt% based on empirical relationships.

3.1.2 The Guatemala Basin

The lithosphere and crust of the Guatemala Basin has been created at the East Pacific Rise over the last 25 Myrs before being subducted in the Middle America Trench (Fig. 3.6). Reconsideration of magnetic anomalies at the southern end of the Pacific and Cocos plate boundary suggested that crust formed at a full spreading rate of ~220 mm/y (Wilson, 1996). This is significantly faster than the world fastest spreading rate (~145 mm/y) for crust forming at ~30°S on the EPR today. In the area, ODP site 1256 has been drilled and revisited two times. So far, it is the only drill site penetrating the layer-2/layer-3 transition zone into the lower gabbroic oceanic crust (Teagle et al., 2012). However, even though site 1256 provides some of the required features of a potential MoHole site, pre-site survey refraction data were rather limited (only 2 to 3 inline OBS). Therefore, data just have been used to yield a 1-D reference crustal structure. Further, MCS data did not show the required clear Moho-reflection of a MoHole site (Wilson et al., 2003) (see above for definition

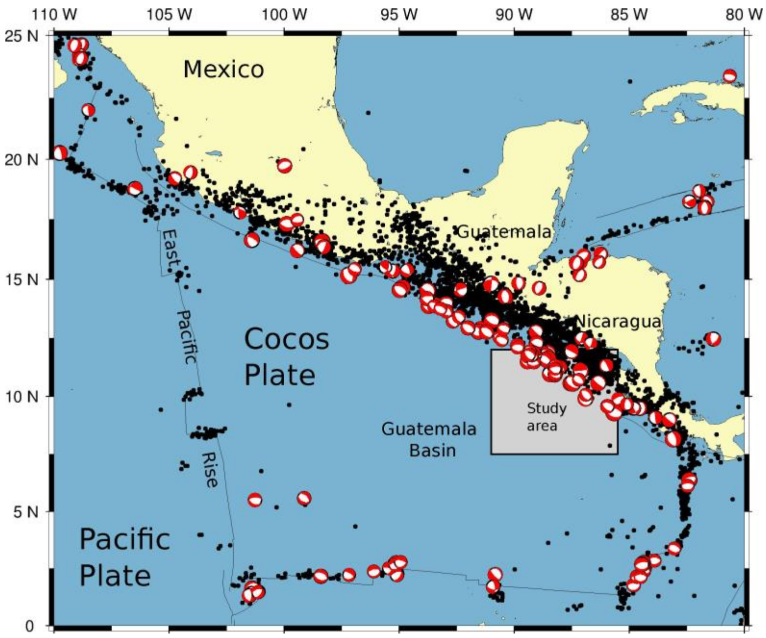

Fig. 3.6 Location map of the study area in the Guatemala Basin and at the Middle America Trench off Costa Rica and Nicaragua. Note, only earthquakes with extensional mechanisms are shows, revealing normal faulting at mid-ocean ridges and bending-related faulting in the trench-outer rise of the subducting Cocos Plate.

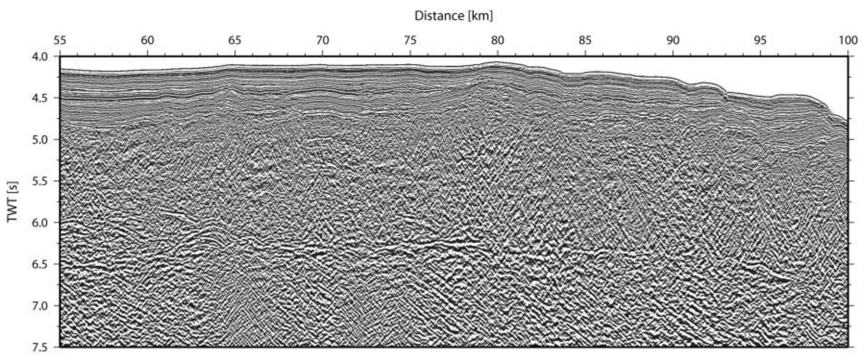

Fig. 3.7 Seismic Moho from MCS data at the westward limit of the trench-outer rise (from Ivandic et al., 2008) where oceanic crust of the Guatemala Basin descends into the Middle America Trench.

of recommended features). Finally, with 15 Myrs the site is just at the thermal limit recommended for drilling (Ildefonse et al., 2010), preferring ages of >15 Myrs.

Pre-site survey data acquired before site 1256 was drilled suggest that Moho reflections were better defined and more continuous farther east, including the area where site 844C was drilled. This feature is supported by seismic data from the trench, where crust in the trench outer rise showed a continuous and well-defied seismic Moho (e.g., Grevemeyer et al., 2007; Ivandic et al., 2008) at about 1.8 s TWT (Fig. 3.8). In addition, seismic refraction and wide-angle data from the trench-outer rise show clear PmP arrivals on basically all OBS stations (Grevemeyer et al., 2007; Ivandic et al., 2008), fulfilling the requirements of a future MoHole site. Crustal thickness from tomographic inversion of seismic refraction and wide-angle data is in the order of 5.5 to 5.8 km and hence well below the mean thickness of 6.5 to 6.9 km reported by White et al. (1992) for the Pacific Basin.

A compilation of heat flow data from the Cocos Plate suggested that heat flow of the entire plate is rather low (Heesemann et al., 2009). Approaching the trench-outer rise, sediment thickness increases and heat flow fraction (ratio between observed and expected heat flow) increases, too, suggesting a decreasing hydrothermal activity with increasing age. However, heat flow surveys conducted in the area between site 1256 and site 844 suggest a rather large variability of heat flow and highlighting the fact that seamounts govern hydrothermal flow through mature lithosphere (Villinger et al., 2017).

Approaching the trench-outer rise indicates bending-related faulting (e.g., Lefeldt et al., 2009) and increased hydrothermal flow caused by bend-faulting (Grevemeyer et al., 2005). Further, joint travel time inversion of seismic refraction and wide-angle data revealed that plate bending is an evolutionary process, causing serpentinization and hence hydration of the mantle prior to subduction (Grevemeyer et al., 2007; Ivandic et al., 2008). Percolation of water into the subduction plate is governed by plate bending, restricting serpentinization to the upper part of the lithosphere that is under extension.

3.2 Aims of the Cruise

Our understanding of the evolution of the oceanic crust and mantle has changed dramatically within the last 15 years. Since the recognition of seafloor spreading and the development of plate tectonics in the 1960s, it became widely accepted that Earth exploration needed to include an oceanic MoHole drilling project with the goal of obtaining a complete section of oceanic crust and underlying uppermost mantle that partially melted to make this crust at a mid-ocean ridge. This goal of sampling intact mantle has featured as a flagship project in all generations of strategic plan for scientific ocean drilling. An in situ MoHole section of oceanic crust and mantle is critical to understand and ground truth the processes by which partial melting and melt-migration beneath a mid-ocean ridge lead to the formation of the oceanic crust that covers about 60% of Earth’s surface. The generation of oceanic crust is a principal geochemical agent in the plate tectonic cycle defining convection and melting of the silicate Earth. For decades, drilling and sampling a MoHole section has been recognized to be a key piece of obtainable knowledge to better understand the chemical evolution of our planet. The discovery of widespread ‘black-smoker’ hydrothermal circulation at mid-ocean ridges in the late 1970s further expanded the rationale for a MoHole to also constrain how hot near-ridge and colder off-ridge hydrothermal alteration transform the oceanic crust by fluid-rock exchange and microbial processes between its igneous birth and eventual recycling into the mantle at an oceanic subduction zone.

This strong scientific driver for MoHole2Mantle (M2M) drilling has been further transformed and enhanced by one of the most important geologic discoveries of the last 15 years – the observation that plate bending near a trench is associated with significant chemical hydration-linked reactions in cold lithospheric mantle and overlying oceanic crust. Bend-faults play a key role in this process, providing high-permeability pathways for seawater to flow into, reach, and react with the cooler portions of lithospheric mantle as the incoming plate bends prior to its subduction. This newly recognized geological process, Bend-fault serpentinization (BFS) has the potential to reshape our understanding of Earth's planetary water and carbon cycles.

The Cocos Plate offshore Central America is unique in that it provides the world's only site where bend-fault serpentinization takes place at seafloor depths of ~3200-3600m, i.e., is the only place at depths accessible to the ~4000m future design limit for Chikyu riser drilling. In contrast, bend-faulting off Japan occurs in water depths greater than 6000m. This region is also unique in that the most promising region for a candidate M2M MoHole drill-site lies next to, and along the same lithospheric flowline as this BFS site. We believe this juxtaposition is a strong scientific argument to favor the Cocos Plate for both BFS and M2M drilling. This is the only region on Earth where we can use ocean drilling as a tool to study the evolution of the oceanic crust and mantle from ridge to trench.

Goals are

1. Mapping variations in the accretionary process over millions of years, revealed by crustal thickness and seismic velocities.

   The oceanic lithosphere is created by seafloor spreading at mid-ocean ridges. However, periodicities in the accretion may affect lithospheric formation. Variations of melt generation and mantle temperature will affect crustal formation, which will in turn affect crustal thickness and crustal velocity structure, most importantly in the lower crust. Crustal thickness and seismic velocity are therefore proxies to assess periodicities in crustal accretion over time. Yet, such variations are poorly studied, but MCS images indicate profound changes over time (e.g., Reston et al., 1999) and even in the vicinity of the fast-spreading East Pacific Rise (Barth and Mutter, 1996; Aghaei et al., 2014).

2. Studying the nature of the seismic Moho as expressed both in wide-angle data (PmP) and in multi-channel seismic data.

   Seismic survey at the East Pacific Rise and in the interior of the Pacific Plate both reveal strong variations in the appearance of the seismic Moho in MCS data (e.g., Barth and Mutter, 1996; Reston et al., 1999). Furthermore, also the seismic Moho or PmP phase in wide-angle seismic lines shows a significant about of variation. Unfortunately, MCS and wide-angle profiles are generally not coincident. Here, we like to study the variability of seismic Moho as expressed in different acquisition methods (MCS vs. wide-angle) and will provide an inventory and reveal features governing the expected variability.

3. Revealing upper crustal velocity structure as a function of plate age and relating changes to the hydrogeological regime as expressed by heat flow data.

   It is well known that upper crustal velocities increase with age and are controlled by hydrothermal precipitation of alteration products into open pore spaces of the extrusive crust. We like to survey the relationship between changes of the seismic properties of the upper crust and the sealing age (hydrothermal mining of heat). Thus, are changes of layer 2 seismic velocity indeed related to the sealing age or does the velocity “saturates” after about 10 Mio. years?
4. Surveying ventilation of The Cocos plate as it descends into the trench and its dependence on seamounts and bend-faults

   Heat flow in the Cocos plate is rather low but increases with age. However, bend-faulting seems to rejuvenate hydrothermal activity near the trench, a process yet not well surveyed and understood. We want to test the hypothesis that seamounts, which control hydrothermal flow in the plate interior, are also “key players” for fluid migration in the trench-outer rise.
5. How far away from the trench does bending-related faulting reach?

   Data acquired in the past (e.g., Grevemeyer et al., 2007; Ivandic et al., 2008) revealed the effects of bending-related faulting and evidence for mantle serpentization at subduction trenches. However, off Nicaragua previous surveys failed to not reveal “normal” mantle at depth (below bend-faulting region) and the onset on bend-faulting. We like to survey the onset and development of bend-faulting and its effects on crustal and mantle properties along the main transect.
6. Collecting the required IODP pre-site survey data for a potential MoHole site.

   In 2010 a workshop (Ildefonse et al., 2010) defined the required features as: (i) simple tectonic setting with very low-relief seafloor and smooth basement relief; (ii) typical Pacific-type seismic velocity structure; (iii) a sharp, strong, single-reflection Moho imaged in MCS data; (iv) a strong wide-angle Moho reflection (PmP); (v) a clear sub-Moho refraction branch (Pn); (vi) a clear upper mantle seismic anisotropy. The Guatemala Basin is one of the proposed settings in the Pacific Ocean where these features may occur and therefore the cruise JC228 is going to collect the required data for defining a potential MoHole drill site.

3.3 Agenda of the Cruise

Seismic profile across Site 1256

ODP hole 1256D is among the deepest drill holes sampling intact oceanic crust and it is the only hole world-wide that penetrated the entire layer 2 (upper crust), reaching lower crustal or layer 3 type plutonic rocks at approx. 1.35 km below the top of the basement. Its IODP legs 309/312 drilled roughly 150 m of dominantly gabbroic rocks. During the ODP and IODP campaigns, down-hole logging provided a unique set of seismic velocities estimates in the upper 1.5 km of the oceanic crust. These data provide an excellent reference to rate constraints from seismic refraction data against logging data. Yet, hole 1256D was drilled at a site with rather limited seismic data coverage, especially lacking seismic refraction and wide-angle profiling. The first profile was therefore designed to cross hole 1256D /Fig. 3.8) to benchmark seismic velocities estimates and reveal crustal thickness at one of the deepest holes ever drilled into an oceanic plate.

Main flow line transect

We proposed to collect a continuous MCS/OBS profile that runs along a flow line from the easternmost extent of MCS profiles acquired during the site surveys for IODP Site 1256 to the trench at the Central American subduction zone (Fig. 3.8).

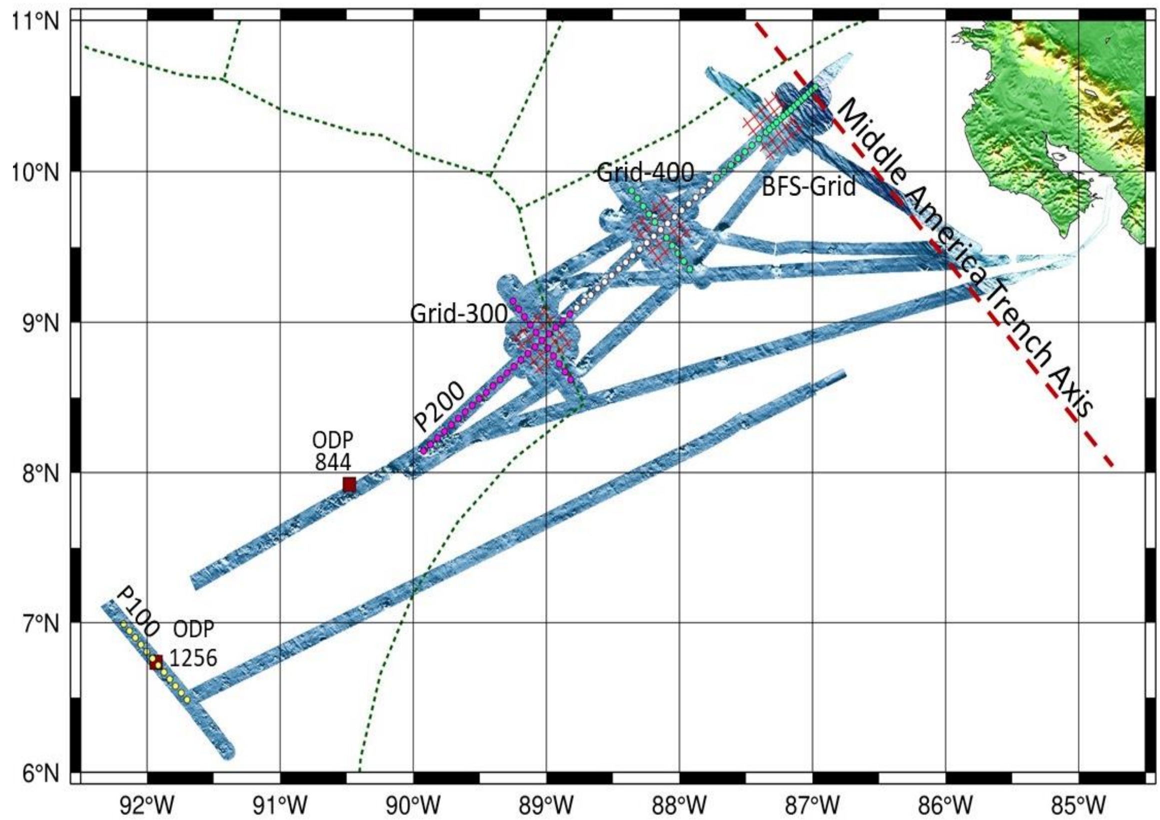

Fig. 3.8 Data collected during JC228 as outlined in 3.3; coloured dots mark different OBS deployments. White dots are OBS223-242 recording shots from both the western and eastern segment of P200 staying for 20-25 days on the seabed; back ground swath coverage from JC228 until 6. January 2023.

We will use this profile to determine whether and how discrete structures evolve as the plate ages – do faults show any change in reflectivity or geometry with age? By careful analysis of offset of different sedimentary reflections, we will measure the variation in fault activity with time, and using this together with swath bathymetry and sub-bottom profiler data we will identify the onset of plate-bending fault activity. We will then determine to what extent the plate-bending normal faults are related to pre-existing structures, whether formed at the ridge axis or as the plate ages. We will also investigate changes in the reflectivity and depth extent of the bend faults as the plate passes through the maximum bending and into the trench. Finally, we will determine whether there are changes in the crustal reflectivity – either in terms of intracrustal boundaries or faults – to be relate to changes in the thermal structure at the ridge as the spreading rate changes. Linking to the previous site surveys in the region allows us to leverage the legacy seismic reflection data to extend the age and spreading rate range over which we can test these changes.

We will determine the variation in seismic velocity structure of the crust and particularly whether and how oceanic layer 2 seismic velocities vary with age in mature crust. This will give a control on the extent to which there may be long-term circulation of fluid within the upper crust as fluid circulation is the primary contributor to changes in the porosity and alteration that control the seismic velocities within layer 2. We will determine whether there are changes in the thickness of the crust and in the properties of layer 3 – this is a significant and rare opportunity to investigate the output of a mid-ocean ridge over several Mio. years. Finally, we will determine the lower crustal and upper mantle seismic structure and its variation with age and location. Specifically, we will test the relationship between the onset of plate-bending fault activity identified from the reflection and sub-bottom profiler data, and reductions in lower crustal and upper mantle seismic velocities that indicate serpentinization due to water penetrating down the pathways provided by the faulting. We will investigate how the intensity of serpentinization varies with depth into the mantle and time since the start of faulting; this will allow us to constrain minimum fluid circulation volumes with time. Refraction profiles are shot at constant 60 s time interval (roughly 150 m shot spacing) and MCS profiles are shot using at 75 m distance spacing (roughly 30 s shot interval). 75 m spacing was preferred over 50 m spacing since there is some evidence that in the 1256 site survey (collected at 50 m) significant energy from the previous shot was still present in the water column.

MoHole grids

At the two candidate MoHole sites (called grid-300 and grid-400; Fig. 3.8), we will use comparisons between the main profile and the perpendicular OBS profiles to determine the degree of crustal and upper mantle anisotropy. Crustal anisotropy, particularly in the upper part of the crust, measured at the ridge axis is attributed to preferential fracturing parallel to dikes and perpendicular to the main spreading; whether this anisotropy persists to mature lithosphere will give constraints on the filling of fractures during hydrothermal circulation. Upper mantle anisotropy is commonly viewed as a proxy for strain accumulated near the ridge axis, so that the magnitude and direction of anisotropy indicates the style of mantle upwelling during formation of the crust. A minimum degree of upper mantle anisotropy is also one of the requirements for suitability for the eventual MoHole drilling.

The two grids of MCS profiles will allow us to determine the 3D nature of crustal reflections and faulting, as well as to establish the degree of variability in these parameters. From the orientation of faults, we will be able to determine whether they are primarily from the East Pacific Rise, or whether they have formed in more complex stress environments away from the ridge. We will be able to compare the reflectivity and its changes at different ages to that previously observed near ODP Site 1256. These MoHole grids will also establish a baseline against which we can compare data from the BFS grid. All grids, including the cross lines with OBS, are shot at a distant-depending spacing and hence 75 m.

BFS site

We are going to use the seismic reflection grid around the BFS site (also called grid-500) to determine the geometry of plate-bending normal faults in three dimensions. This will enable us to test more completely whether the plate-bending faults develop from inherited structures on the incoming plate or whether they are newly formed. We will be also able to determine variability along and across strike in their reflectivity, depth extent, and offset. These profiles will document whether and how the orientations and properties of bend faults change during the lithospheric buckling before subduction.

The Autosub bathymetry data would have been an important tool to map in detail the surficial geometry along and between the up to ~40km-long plate-bending faults. Because Autosub flies close to the seabed (~150m altitude) it allows the use of a high-frequency swath system that has ~10-20 times better resolution than best shipboard systems (~1m lateral resolution). This is sufficiently small that we expect to be able to identify any zones of focused upward fluid flow in the form carbonate pavements or even mounds or chimneys. The backscatter data from both the multibeam bathymetry system and a concurrently used sidescan sonar would allow locating areas of younger or more diffuse fluid flow that have led to seabed sediments becoming cemented or just showing the presence of bacterial mats or macrofauna. Bathymetric expressions of venting, in concert with water column measurements such as temperature and conductivity are critical to yield the presence of fluids that have reacted with warm/hot rock at depth. A photographic AUV-mission would allow potential vent sites to be characterized in more detail, to determine whether venting is ongoing, and to identify any chemosynthetic macrofauna that may be present. The combination of methods will enable us to locate sites where it may be possible to sample fluids that have passed through a BFS reaction zone. Pore waters from sediment cores will yield initial hydrothermal fluid characteristics.

We will use the heat flow measurements along with the evidence for seafloor fluid venting to test models of subsurface fluid circulation through the BFS systems. Heat flow measurements around plate bending faults have already documented that there is a circulation pattern involving intense fluid inflow into the seafloor above the region of BFS. However, data are very sparse. We will take additional measurements to constrain the along-strike continuity of this circulation pattern, and identify, and if possible, sample, the much smaller targets associated with hydrothermal outflow.

4 Narrative of the Cruise

4.1 Leg 1

On the 7th of December 2022 the RRS JAMES COOK left its berth in Caldera 6 p.m. local time, tackling its expedition JC228 to survey the structure of oceanic crust in the Guatemala Basin and in the deep-sea trench off Costa Rica and Nicaragua. Please note that all operations were either conducted in Costa Rican or international waters, though a permit for Nicaragua was available. The request for permits was intended to allow maximum flexibility in planning. However the guard boat required for the 6 km streamer was not allowed to operate in Nicaraguan waters, hence the seismic profiles needed to lie solely within Costa Rican waters. In general, weather conditions throughout the survey were very good, although winds were consistently higher at the eastward end of the survey. Leg 1 terminated on the 9th of January at 7 a.m. local time.

Leg JC228A narrated day by day:

30.11. to 07.12.2022: Port call of RRS JAMES COOK in Caldera, Costa Rica; port logistics and mobilisation of equipment; scientific party arriving on the 3rd of December.

8.12.2022: Leaving port after 30 hours delay at 0:00 UTC (7.12.2022 1800 local time). After MMO period recording of underway geophysical data acquisition from ~13:00 UTC onwards; 16:25 to 21:30 UTC CTD measurement (down to 3 km) to obtain sound velocity profile for the EM122 Kongsberg echosounder and releaser test; second releaser test (down to 1 km); underway geophysics after MMO. Safety drill in the afternoon at 4 p.m. local time.

9.12.2022: Releaser tests between 15:30 and 20:15 UTC (three dips down to 1 km); underway geophysics after MMO.

10.12.2022: 7:50 to 13:36 UTC deployment of 12 OBS along profile P100 across ODP/IODP site 1256; 16:30 to 20:30 UTC airgun & magnetometer deployment; MMO, soft start; 20:37 UTC: first shot at 60 s interval along P100.

11.12.2022: 08:06 UTC: last shot, magnetometer, airgun recovery – on deck at 11:27 UTC; 13:44 UTC first station OBS112 released; recovery of OBS continued.

12.12.2022: 00:37 UTC: recovery completed (12 OBS) and last OBS101 on deck; 01:03 to 14:30 UTC: transit & underway geophysics, incl. magnetics; 15:03 UTC: begin deployment of 42 OBS along western part of P200; OBS201 to water; OBS deployment continued.

13.12.2022: OBS deployment continued; 3:04 UTC OBS242 deployed; transit to P300 with underway geophysics, incl. magnetics; 22:34 UTC OBS301 deployed.

14.12.2022: OBS deployment continued; 06:39 UTC OBS310 deployed; 12:03 to 18:56 UTC tail buoy & 6-km streamer deployment & balance test; 19:44 to 21:19 UTC gun deployment & MMO; 21:35 soft start & test of seismic streamer for multi-channel seismic (MCS) profiling along profile P199.

15.12.2022: turn onto line P200w; 03:28 UTC first shot at 60 s for OBS wide-angle (WAS) profiling.

16.12.2022: 06:45 UTC last shot at 60 s for WAS; change of shot interval to 30 s for all turns and 75 m for MCS lines; 10:14 UTC: first shot along eastern section of P200mcs

17.12.2022: 00:45 UTC change from P200mcs onto easternmost seismic grid “300”; 2:15 on line 352; 9:50 on line 301; 16:33 on line 302.

18.12.2022: continuing shooting seismic grid; 8:16 on line 300; 20:27 stop of shooting during turn and maintenance of guns; 22:37 guns back and shooting after MMO; 22:45 on line 303.

19.12.2022: continuing shooting seismic grid; 8:15 on line 304; 15:18 on line 354; 21:04 on line 353.

20.12.2022: 00:45 UTC medical incident requires immediate termination of seismic profiling and return to port; 00:53 last shot & recovery of magnetometer, airguns & streamer; commence passage to Caldera for medical emergency, transit with three engines at 14-15 kn; underway geophysics.

21.12.2022: 03:00 UTC rendezvous with pilot off port of Caldera; patient leaves vessel; 03:15 UTC return to working area at 10-11 kn; underway geophysics & magnetics.

22.12.2022: OBS recovery eastern 22 stations from P200 and 10 OBS from P300; 10:14 UTC first OBS201 on deck; OBS recovery continued.

23.12.2022: OBS recovery continued.

24.12.2022: 01:38 last OBS310 on deck, recovery of 32 OBS completed; 02:20 UTC transit and underway geophysics with magnetics; deployment of 10 OBS along P400 and 22 OBS along the eastern segment of P200; 08:32 UTC first OBS410 deployed.

25.12.2022 02:47 UTC last OBS264 deployed; 03:27 UTC SVP – measurement of sound velocity profile at deep-sea trench; first day of the cruise where research activities were hindered by weather and sea conditions. A strong wind with 20-30 kn from northerly direction from Nicaragua and a strong current roughly paralleling the trend of the trench axis (SE-NW) affected the operation of towed equipment. We therefore had to run the seismic refraction profile shot at 60 s without the 6-k streamer; 10:22 deployment of airguns & magnetometer 30 nm eastward from OBS264 and MMO at sun rise; 12:57 UTC soft start; 13:13 UTC first shot at 60 s for eastern part of WAS profile P200e.

26.12.2022: 17:55 UTC last shot along P200e; recovery of magnetometer and airgun arrays; transit and underway geophysics to streamer deployment for MCS along the eastern segment of P200mcs and the second grid “400”, shot with a spacing of 75 m along straight lines and 30 s in all turns.

27.12.2022: 2:50 UTC begin streamer deployment; 7:30 streamer deployed; 10:19 UTC all airgun strings deployed; 13:01 UTC soft start after MMO; 13:27 UTC MCS profiling along p200mcs continued; 23:18 UTC last shot on P200mcs and turn onto second grid “400”.

28.12.2022: 00:56 UTC first shot along P452; 8:35 UTC on P451; 21:29 UTC on P403.

29.12.2022: 9:30 UTC on P400; guard boat indicated problem with engine and had to steam towards Puntarenas; it was decided after communication with UTM (owner of streamer) to commence with seismic operations in the area of the second grid without any fishing activity and little ship’s traffic; 22:04 UTC on P402.

30.12.2022: 02:18 UTC termination (last shot) of operation due to emergency call from guard boat about 70 nm from our current position where its engine failed; 04:24 UTC all airguns recovered; 10:28 UTC streamer and tail buoy recovered; transit to position of call of distress; 14:00 UTC arriving at guard boat, tow towards Nicoya Peninsular and hence meeting point with tow boat.

31.12.2022; 6:21 UTC tow completed, heading towards OBS253; recovery of 12 OBS in near trench area; 16:26 UTC OBS253 recovered; recovery OBS254-261 continued; 23:00 UTC OBS262 recovered.

01.01.2023: 00:00 UTC OBS263 recovered; 1:15 UTC OBS264 recovered, recovery of 12 OBS completed; move for swath & magnetometer profile; 2:35 UTC magnetometer deployed 390 m beyond stern.; 10:40 UTC arriving at OBS410; 11:28 UTC OBS410 recovered; 14:58 UTC OBS406 recovered and transit to OBS223; 20:45 OBS223 recovered; 23:19 OBS225 recovered.

02.01.2023; 00:40 OBS226 recovered; recovery OBS227-232 continued; 08:15 OBS233 recovered; OBS234 left on seabed to record shots to be fired on second grid; 10:08 UTC last OBS235 recovered, recovery of 17 OBS completed; onset of rain and heavy showers, but calm sea state; 10:40 UTC tail buoy of streamer deployed; 15:02 UTC 6-k streamer deployed; 15:05 UTC start airgun deployment; 16:55 UTC all guns in water; 17:54 UTC soft start after MMO and continuation of shooting second seismic grid “400”; 18:33 UTC on line P450; decaying activity of showers.

03.01.2023: 3:32 UTC on line P455; 14:05 on line P401; 18:00 UTC stop shooting seismic grid; guard boat won’t be available for the remaining survey. Therefore, due to safety reasons the length of the streamer must be shortened to 3-k before continuation of P200mcs and approaching the deep-sea trench. Its closer proximity to the coast may result in a higher density of ship’s traffic and fishing activity; 22:21 UTC streamer reduced to a total length of 3-k; soft start after MMO.

04.01.2023: 6:01 UTC on 200mcs; 21:35 UTC last shot and turning onto BFS grid or grid “500”.

05.1.2023: rough sea and wind of up to 25 kn; continuing shooting BFS grid.

06.01.2023: 5:09 UTC last shot on BFS grid; 5:33 UTC begin airgun recovery; 7:50 all airguns on deck; 10:40 UTC streamer and tail buoy recovered; sunny weather but with strong wind and rough sea conditions of up to 2 m of waves; OBS recovery of OBS252-236, OBS234, and OBS405-401; 15:22 UTC OBS252 on deck; OBS recovery continued in westerly direction; with increasing distance to coast wind and sea state gets calmer.

07.01.2023: OBS recovery continued.; last OBS401 recovery at 21:33 UTC; all 96 OBS deployments conducted during the survey were successful and provided data of excellent quality for geophysical exploration; deployment of magnetometer to conduct an additional magnetic line paralleling the main corridor.

08.01.2023: magnetometer at 11:45 UTC recovered; transit to Caldera after concluding geophysical underway measurements.

09.01.2023: 07:00 RRS JAMES COOK at berth; port logistical operations issued.

4.2 Leg 2

Between leg1 and leg 2 several large equipment such as the OBS, the seismic streamer, and the airgun-array had to be unloaded while the AUV and the coring system had to be loaded onto the vessel. In the meantime, a partial exchange of the scientific party also took place. By late afternoon on January 12th all equipment and scientific personnel was onboard, and leg 2 or leg B of cruise JC228 was ready to start.

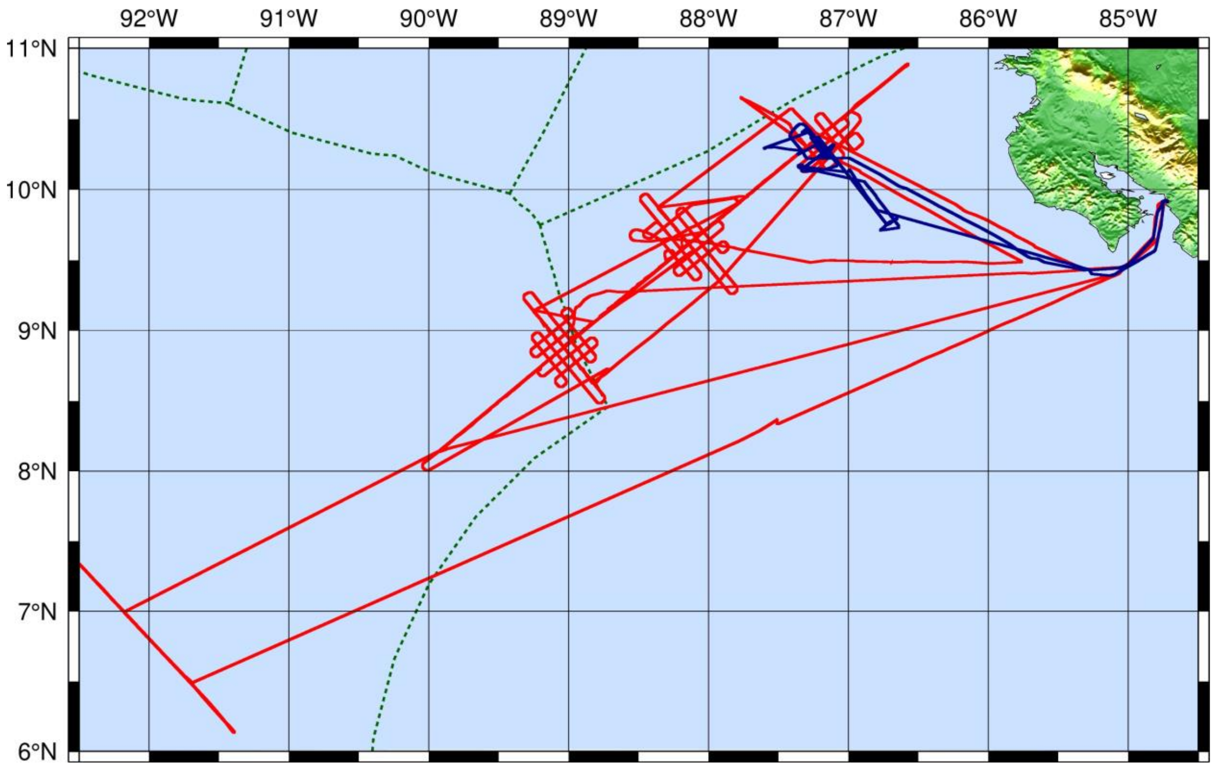

Fig. 4.1 Track chart of JC228 (red: leg 1; blue: leg2). The survey and all legs were operated from the port of Caldera in Costa Rica.

Leg JC228B narrated day by day:

10.-12.01.2023: RRS JAMES COOK at pier in Caldera, Costa Rica loading and unloading 6 and 5 containers, respectively.

13.01.2023: At 06:56 LT RRS JAMES COOK had to vacate the berth at the pier and DP'd in bay for final preparations. AUV swim test 19:22 – 19:41 UTC. Ship sailed at 19:51 UTC for the study area. Safety drill at 16:15 LT., Calm sea and light breeze.

14.01.2023: First station (6-m long gravity core) taken at 13:32 UTC. Core intended for background porewater profile and to test depth of penetration for spacing of the heatflow probes on core barrel. Weather conditions deteriorating (wind gusts up to 25 kn and 2-3 m waves) and too poor for AUV launch. Deployment of magnetometer at 15:51 UTC. Determined that 6 m penetration was possible and the core barrel for heatflow measurements was modified to match.

15.01.2023: Magnetometer survey aborted at 01:20 UTC. First heatflow profile from 02:37 to 11:56, then coring with 12-m gravity corer (excellent recovery). Third core attempt abandoned due to wire of corer frame snatched by ship's propeller. Strong surface currents preventing empty corer frame to remain vertical. No damage to propeller, but winch on davit of corer frame not usable anymore. Weather conditions (windy and rough seas but sunny) still too poor for AUV launch.

16.01.2023: Second heatflow profile crossing several bend faults closer to the seamount running from 01:05 UTC until 12:16 UTC. Overnight sea state improved allowing AUV deployment at 13:19 UTC. AUV not diving but had shut down WiFi at start of survey plan. Communication with vehicle not possible. Initially vessel following AUV, then coring with 9-m and 6-m gravity corer. Deployment without corer frame.

17.01.2023: Third heatflow profile between 02:08 and 13:50 UTC then pick up AUV at 16:20. Problem for non-diving was too much buoyancy of the vehicle. Two gravity cores NW of volcano, then floating test of AUV.

18.01.2023: Fourth heatflow profile between 01:09 and 13:32 UTC then second attempt at AUV mapping at 15:19 UTC. Vehicle tail-heavy would not dive, vehicle damaged during recovery at 17:00 UTC. Two successful coring attempts on top of volcano, then moving SSE with underway geophysics.

19.01.2023: Fifth heatflow profile between 04:32 and 17:16 UTC, followed by 9-m core that over penetrated. Bathy survey back to previous work area.

20.01.2023: Sixth heatflow profile between 04:22 and 12:06 UTC, followed by two 3-m cores recovering possible fossil fragments. Short survey for SBP, then transit and seventh heatflow profile. At the last heatflow station collected, the cone at the base of the core barrel was replaced with a conventional core cutter and a core was collected simultaneously with the temperature profile.

5 Instrumentation / Data acquisition systems

5.1 Shipboard EM122 Kongsberg swathmapping echosounder

The RRS JAMES COOK is fitted with a Kongsberg EM122 1°x2° multi-beam deep ocean echosounder, with two transducer arrays fixed to the ship's hull operating at 12 kHz. Data acquisition is based on successive transmit-receive cycles of this signal. The transmit beam is up to 150° wide across-track and 1° along-track direction. The system has 432 beams, sampling seafloor depth at high resolution. The equidistant beam spacing was used. For the first part of the cruise the maximum recorded angles were set to 60° to each side of the vessel, however the relatively poor performance of the outer beams and the line spacing within the survey grids meant that the maximum angle was changed to 55°. Seabed depth and reflectivity are recorded against UTC and GPS location. The raw depth data are processed to obtain images of the seafloor, including depth contour maps, and the acoustic amplitude processed to obtain backscatter amplitudes. During the cruise bathymetric data were cleaned, editing raw swath data either with MB-System or with Caris HIPS Software. Tests about the resolution of the EM122 revealed that bathymetric grids with a footprint of 50 m could be obtained, and potentially 25 m in limited areas.

5.2 Ocean-Bottom-Seismometers

During the survey two types of ocean-bottom seismographs where deployed. The UK OBSs were provided by the UK's Natural Environment Research Council's (NERC) Ocean-Bottom Instrumentation Facility (OBIF). Thirty LJ1-type platforms were available for 45 deployments during the cruise. These instruments were four-channel OBSs that record to microSD cards, and were configured to record both three-component geophone (Sercel L-28 4.5 Hz) and hydrophone (HiTech HTI-90-U) sensor data. Data were digitized within the datalogger at 24-bit resolution at a sampling rate of 500 Hz. Buoyancy of the OBIF OBS is provided by four small glass spheres, which limits their depth of operation to a water depth of <5500 m. Like all the other OBSs, these instruments are released using acoustic communication. Fig. 5.1a shows an OBIF OBS ready for deployment on deck of the COOK.

GEOMAR OBS were of the so-called design-2002 (also named drum or roller type OBS after the shape of the buoyancy) or "LOBSTER"-type OBS; in total twenty-four instruments were available. However, we only deployed up to twenty-two in the same deployment, but remaining stations were already prepared for the next deployment to minimize the "turn-around" time while moving from one seismic line to the next profile. Some stations were deployed up to three times during JC228. The OBIF' OBSs, GEOMAR's stations were also equipped with a geophone and a hydrophone. The hydrophones were HTI-90U from High Tech Inc.; geophones where 4.5 Hz SM6 B-coils in a pressure protected housing manufactured by KUM GmbH, Kiel, modified from a package designed by Carrack Measurement Technologies. Recording units were of an in-house design of 32-bit seismic data logger, called Geolog. We recorded the hydrophone output on two channels (channels 1 and 5) at two different amplification levels providing well-amplified long-range records (gain 16) and preventing clipped amplitudes from short-range airgun shots (gain 1) to minimise difficulties with amplitude restoration because no gain range was implemented. The gain for seismometer channels 2, 3, and 4 was set to 16, which provided good signal-to-noise ratios for all record offsets without clipping of amplitudes. The Geolog was set to a sampling rate of 250 HZ and the timing was controlled either by an atomic clock or by a temperature compensated clock (SEASCAN). As for the UK' OBSs, GEOMAR used separate pressure housings for the acoustic release and seismic data loggers. Buoyancy was provided by syntactic foam. Most OBSs were rated to 6000 m water depth, though the LOBSTER-type OBS were rated to 8000 m. However, the deepest OBS to be deployed during the cruise was "only" at 5010 m (OBS264) at the axis of the deep-sea trench. Figs. 5.1b and Fig. 5.1c show a GEOMAR-type OBS before deployment. Additional images of OBS operations are shown in Appendix 12.

Fig. 5.2.1 Types of Ocean-Bottom-Seismometers used during the survey

All OBS, regardless of type or supplier, were synchronised to GPS-derived UTC time before deployment and after recovery and the data corrected for clock drift prior to conversion to SEG-Y format.

In total, 96 deployments were made throughout the cruise. OBIF and GEOMAR deployed 45, and 51 OBSs, respectively. However, 15 OBIF OBS and 5 GEOMAR stations remained on the seabed for the entire cruise. These stations were at the centre of the main transect p200, recording shots from the "western" segment (p200w) and the "eastern" segment (p200e). Along the first line p100, we only deployed GEOMAR OBS. All OBS had a perfect run; all OBSs recorded data suitable for geophysical data analysis and all OBSs were recovered safely after released from the seabed. The longest recording period was for OBS234 with 24 days.

5.3 Seismic streamer

The Sercel SEAL streamer (Figs. 5.3.1 & 5.3.2) had a nominal active length of 6 km with 150 m sections. During the initial deployment significant damage was seen on the outside of one of the sections which was subsequently removed. Thus, the active length was 5.85 km with 468 channels at 12.5 m group spacing although the far offsets were still close to 6 km due to the long lead-in. The streamer was towed at a depth of 12 m to keep it below wave disturbance and to enhance low frequencies in the recorded data. Nautilus depth controllers were used with control units inserted into the streamer during the first deployment.

Towing Offsets

From…	…To	Distance (m)
Central reference point (CRP)	Stern	46.1
Stern	Centre of Source (COS)	50.0 ± 5
Stern	Centre Near Group (CNG)	209.6 ± 2.2
Central reference point (CRP)	Centre of Source (COS)	96.1 ± 5
Central reference point (CRP)	Centre Near Group (CNG)	255.6 ± 2.2
Centre of Source (COS)	Centre Near Group (CNG)	159.4 ± 7.2

	Depth (m)
Source	8
Streamer	8

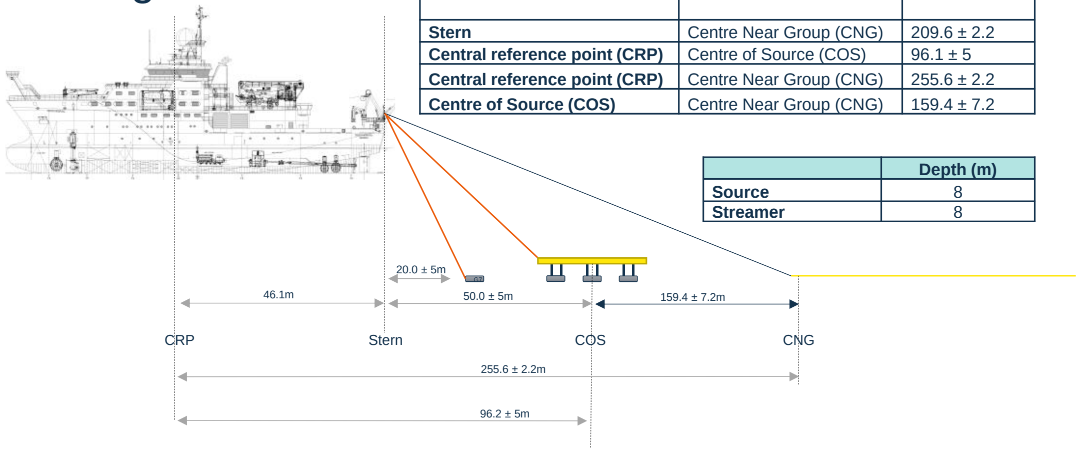

Streamer Head

	Length (m)
Stern – Tail of leadin	186.24 ± 2
SNS	0.72
HAU	0.32
SHS	6 ± 0.2
HESA	10.0
Head of Streamer - CNG	6.25
Stern - CNG	209.53 ± 2.2

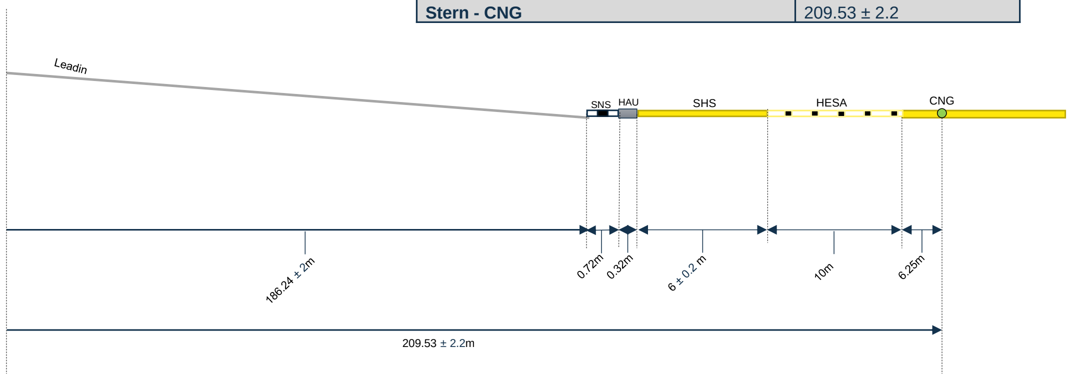

Streamer Tail

	Length (m)
TAPU	0.45
TES	50 ± 1
STIC	25 ± 1
Swivel	0.20
Tailbuoy Chains	1.55
Tailbuoy front - GPS Pod	1.20
Head of TAPU – GPS Pod	78.4 ± 2

	Height above water (m)
TailBuoy rGPS Pod	1.6 ± 0.25

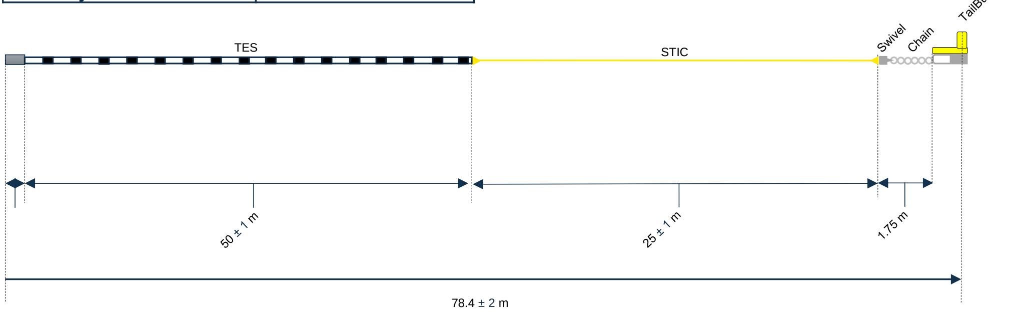

Fig. 4.3.1 Layout of the seismic streamer / National Oceanography Centre, National Marine Facilities

The streamer was weighted during the initial deployment based on the expected temperature and salinity conditions, and a trial stabilization test was carried out with half of the streamer deployed which showed that it was towing evenly with limited input from the depth controllers. The winches and most of the streamer sections were supplied by the Spanish CSIC, although some of the sections came from the NERC streamer, as well as the main HAU unit which was an x028 configuration. Seventeen (only nine for the streamer reduced to 3 km) compass units with integrated Streamer Retrieval Devices were deployed on standard bird coils. The tailbuoy used a GPS unit, relaying data over a radio link to the vessel. See Figure 5.3.1 for a detailed streamer and airgun layout.

Fig. 5.3.2: Sercel streamer and a bird during deployment.

Data were recorded in generic SEGD v1.0 format, with 6 auxiliary traces – the shot instant trigger, the time break hydrophone in the streamer head section, and 4 hydrophones from the airgun source array. Sercel recordings start 150 ms before the shot instant.

The streamer generally worked well, although persistent problems were experienced with communications with the two depth controller units closest to the tail. This may indicate some kind of internal damage to the sections between these birds and the next one on the streamer. When changed from a 6 km configuration to 3 km, the lead-in needed to be shortened from 186 m by about 50 m; the lead-in is the main part of the streamer that is negatively buoyant, and the reduced towing drag from the shorter streamer meant that the front part of the streamer was towing at around 20 m depth. See Appendix 12 for images of the streamer system before and during deployment.

5.4 Airgun source

The airgun source consisted of 13 Bolt LL guns, deployed as sets of 3 guns hung from an I-beam plus a single towed gun (see Figures 5.3.1 and 5.4.1 and Table 5.4.1). The total array volume was 5000 in^3, fired at a nominal 2000 psi. The planned tow depth was 9 m. Shots were fired using a Bigshot source controller. Depth sensors at each end of the beams were logged via the Bigshot into the seismic data stream. Pressure was measured in real time at each of the umbilical winches, recorded via the main data logging system, and displayed on a monitor in the

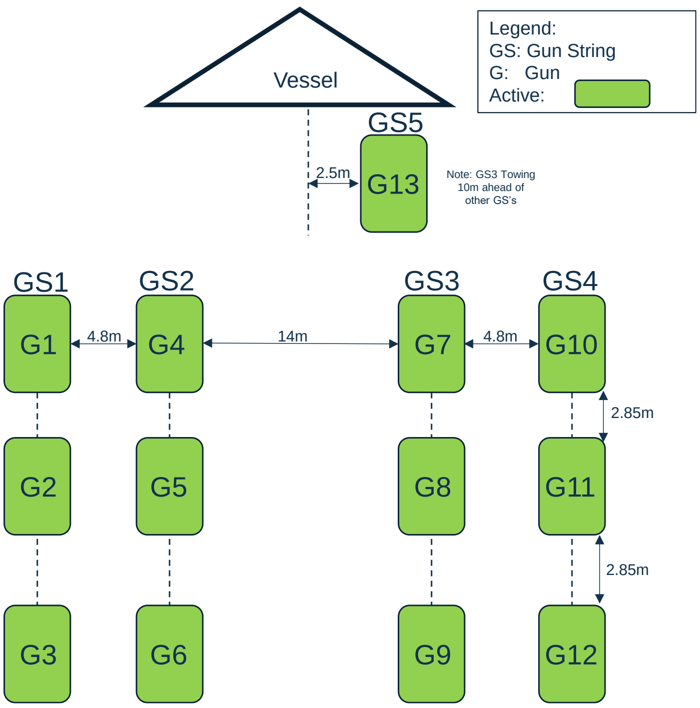

Fig. 5.4.1 Layout of the airgun array / National Oceanography Centre, National Marine Facilities

seismic operations area. A hydrophone at the centre of each beam was recorded on an auxiliary channel on the Seal recording system. Shot instants were logged on the OBIF GPS clocks, as well as the Triggerfish navigation controller and the Seal system.

The source performed satisfactorily during the cruise, although the seismic deployments were cut short due to emergencies that required stopping operations. There were problems with the chains from which the guns were hung – several of these chains failed in use, and in one case a gun was attached only by the air hose and solenoid cable at the time of retrieval. The larger guns (500 in^3) were particularly affected by failures of the chains or pressure hoses, which is assumed to be due to the large recoil of these guns. The real-time display of air pressures is a key advance over previous projects, and allowed the watchkeeping team to rapidly identify failures of hoses. The tow of the airgun beams consistently caused concern. Due to the wash of the ship, the pairs of beams on each side were frequently much closer to one another than the 4.8 m separation of the tow points. In addition, when the ship crabbed to maintain course when affected by wind or current the airgun array consistently came close to the streamer lead-in, even when on a straight profile. See Appendix 12 for images of the airgun system before deployment.

Gun Configuration

Gun String	Gun	Volume	Status	Depth Sensor	Hydrophone Sensor
GS1	G1	300	Active	Yes	No
	G2	400	Active	No	Yes
	G3	500	Active	Yes	No
GS2	G4	250	Active	Yes	No
	G5	300	Active	No	Yes
	G6	400	Active	Yes	No
GS5	G13	700	Active	No	No
GS3	G7	250	Active	Yes	No
	G8	300	Active	No	Yes
	G9	400	Active	Yes	No
GS4	G10	300	Active	Yes	No
	G11	400	Active	No	Yes
	G12	500	Active	Yes	No

Tab. 4.1 Chamber volumes of the airguns in the source array / National Oceanography Centre, National Marine Facilities

5.5 TriggerFish software

Triggerfish navigation software was used to trigger airgun shots and estimate the geometry of the streamer for each record using a combination of the compass sensors and the relative position of the tailbuoy. Profiles designated for streamer recording were prepared with a navigation pre-plot at 75 m shot spacing. Profiles designated for OBS recording and the turns, for which shooting is more useful on the OBS than on the streamer, were triggered at constant time intervals of 60 s and 30 s respectively. The raw Triggerfish output are available as XML files, but were processed into UKOAA P1-90 files (3D format) that can be applied to the SEGD recordings to give precise geometry for each shot.

This was the first NERC cruise to use Triggerfish. The capability to shoot on distance is a good enhancement of what could be achieved previously. The capability to both monitor streamer geometry during acquisition and to easily process the "true" streamer geometry (including curvature as well as feathering) are important when using a 6 km streamer. Equally there were some problems during use including frequent crashes of software components resulting in lost shots or lost records. To use it effectively requires some additional experience from both the seismic operators and the science party, particularly around generating appropriate pre-plot files for the planned profiles.

5.6 Marine gravimeters

A LaCoste Micro-G marine gravimeter (serial number S84) was run throughout the cruise. This meter was provided by the NERC's National Marine Equipment Pool (NMEPA tie-in was performed in Caldera at a reference point (CALD) just outside of the port which was established by Dr Oskar Lücke of the University of San Jose at (9.910097°N / 84.717245°W). Base station ties were completed using a portable LaCoste-Romberg land gravimeter (model G-484). The marine meter, located in the at the centre of the vessel on the main deck, was provided with a NMEA navigation stream from the ship's network and provided data in real time to the TechSAS data logging system. There are potential issues with the data quality when the vessel has significant motion. During the survey gravity field measurements were obtained providing continuous measurements from port to port.

A Dynamic Gravity Systems AT1M gravity meter (S/N AT1M-12U) was located in the same space in the vessel. This is a more recent development of the Lacoste zero-length spring meter. Unfortunately, the real-time data feed is limited, requiring post cruise processing.

5.7 Marine Magnetometer

A SeaSpy2 Overhauser effect magnetometer (SN 14043) of the NERC's National Marine Equipment Pool (NMEP) was deployed throughout all seismic surveying and along additional transit profile from the port of Caldera into the survey area and during longer transits within the study area. The magnetometer was towed 270 m behind the stern of the vessel and thus the sensor lay-back from the ship's GPS reference point was input into the data acquisition "BOB" software. Unfortunately the navigation calculations for the BOB software were not completely reliable, hence the layback was applied during post-processing when the IGRF13 predicted magnetic field was removed. Data acquired during transits and while shooting the airguns only are of high quality, but during some of the seismic profiles when the streamer was deployed the data have spikes of a few seconds duration or magnetic field offsets that last for up to a few minutes. Discussion with Marine Magnetics during the cruise indicated that these represent genuine changes to the measured magnetic field rather than equipment failure. Most likely given the association with the streamer deployment they are due to the magnetometer getting close enough to the streamer to be affected either by physical components or by the magnetic fields generated by the down-streamer power supply currents.

5.8 Shipboard sediment echosounder

The sediment echo sounder is a Kongsberg SBP27, which uses the same transducers as the EM122 multibeam bathymetry system. The transmitted waveform was a 2.9-7 kHz Chirp, initially using a 5 ms sweep, but later changed to a 10 ms sweep. The data are recorded with three receiver beams, each of 3° beamwidth. Data were recorded in SEGY format, both as raw waveform and as processed (correlated, instantaneous amplitude, automatic gain control) data. Positions in WGS84 coordinates are stored in the trace headers at the time of acquisition. During post-cruise interpretation it was discovered that a small fraction (1 ping per 1000 or so) of the pings had lost the sign information for the longitude. This has been corrected in post-processing.

5.9 AUV AutoSUB5

Autosub5 (previously Autosub 2000 Under Ice Phillips et al. 2020) is a high-power work class 6m 2t AUV. It consists of a free flooded nose section containing sensors, a centre section of syntactic foam (the buoyancy) and batteries, the aft section is also free flooded containing navigation, additional sensors and the vehicle control in the form of twin thrusters and 4 independent fins. Its primary objective is to be launch from a ship such as the RRS James Cook to image the seabed in high resolution by operating multibeams used for topographic mapping, sidescan sonars used for acoustic imaging of the seabed, sub bottom profilers use to see what is in the first few meters under the seabed and camera systems.

Fig. 5.9.1: Picture showing Autosub 5 vehicle on gantry before launch.

Other standard sensors include the ADCP for water column tracking and CTD (conductivity temperature depth). Specifically, for this cruise and upcoming cruises it has been fitted with the ROCII EDNA sampler, a magnetometer and a single channel fluorometer. The vehicle has been designed by the NOCs Marine Autonomous robotics division to suit the needs of UK science with the primary goal being modularity so new experimental sensors can be accommodated.

Sensor	Manufacturer	Operating parameters	Purpose
2205 Sidescan Sonar	Edgetech	120kHz 400kHz	Dual frequency sides can imaging
2205 Sub Bottom Profiler	Edgetech	2-16kHz	
WBMS Multibeam	Norbit	200kHz 400-700kHz	Bathymetry mapping, water column data and snippet data.
WBMS Speed of Sound	Norbit		Speed of sound sensor
WBMS Forwards looking Sonar	Norbit	200kHz 400-700kHz	Obstacle avoidance system
Seabird 9+ Dual CTD	Seabird		2 x Conductivity sensors 1 x pressure sensor 2 x temperature sensors
CTD 9+ Dissolved Oxygen sensor	Seabird		
Downwards Cameras	NOC		3m Altitude camera surveys duel flash.
Chip scale Atomic Clock	Microsemi	1pps & NTP	Timing & triggering co-ordination
Sprint Nav 700	Sonardyne	600Khz DVL	Navigation & ADCP Data
Seabird BDRT Ecopuck			
1540 Magnetometer	Applied Physics Systems / NOC		Magnetometer

Tab. 5.9.1 Autosub5 Sensor Fit

Autosub5 has completed 7 weeks of testing in Loch Ness, Scotland. During the Lock Ness trials, the vehicles control system and integration of core payloads (MBES/Sidescan/Camera) were tested from a shore facility in up to 220m of fresh water. Following the Loch Ness trials, a 3-week sea expedition DY152 (July 2022) was carried out to fully commission the vehicle for science deployments. During DY152 Autosub 5's primary objects were completed confirming it could be launched from a ship and dive to 4200m. Additionally it completed some initial science objectives by completing the Greater Haig Fras survey and an overnight multibeam at the very bottom of Whittard Canyon which was a repeat of Autosub 6000 mission 100. The configuration used during JC228B is indicate in Tab. 5.9.1.

5.10 Coring and porewater sampling

Fig. 5.10.1: Porewater sampling

A standard marine gravity corer with plastic liners was used together with a corer deployment frame. Two sets of barrels with 3-m and 6-m length were available, resulting in possible corer lengths of 3, 6, 9, 12 and 18 metres. After damages to the corer frame and the motor on its davit, the corer frame was no longer functional, restricting possible corer lengths to 3, 6 or 9 metres. Cores have a diameter of 12 cm and porewater sampling was carried out using Rhizon samplers. Porewater was tested onboard for pH.

5.11 Heat flow probe

During this cruise we used autonomous temperature loggers (MTL) mounted onto a 6 m long core barrel. The lower end of the core barrel was closed so that we could do multi-penetration stations (pogo-style). The MTL are built by Antares-geo.com and they are capable of 600 bar ambient pressure. The resolution is about 1 mK while the accuracy is +/- 0.1°C. We used six MTL on the core barrel and one on the top to monitor the bottom water temperature. To take advantage of the high resolution of the individual MTL, we take a calibration time at about 2900 m water depth at the beginning of each station. The data reduction and conversion from time series to temperature-depth profiles is done, using our program-set MHFRed, calculating the heat flow according to Villinger and Davis (1987).

Fig. 5.11.1: Gravity corer with MTL mounts, welded onto the core barrel.

Thermal conductivity is the physical property necessary to calculate heat flow. It is measured on core material of near-by located gravity cores. We decided to take measurements every 20 cm. A commercial physical property analyzer is used (KD2 Pro, Decagon Devices). The KD2 operates according to the pulsed needle probe method (Lister, 1979). We use a 6 cm long needle on whole rounds.

Winch speed for penetration of the heat probe is 1.0 m/s for maximum penetration into the sediment. Time for equilibration to in situ temperatures is assumed to be 7 minutes. The mean duration of one measurement, including transit of approximately 0.3 – 0.5 km between waypoints, is about 1 h per single point of measurement. A Teledyne USBL transponder, mounted on the head of the gravity corer allowed monitoring the position accuracy. This worked excellently in the prevailing water depth of 3000 m.

6 Preliminary Results

6.1 Bathymetric swath mapping

6.1.1 Ship-board bathymetric swath mapping

The EM122 swath mapping sounder of the RRS JAMES COOK operated well during the entire survey, though a small bias between port and starboard beams was observed and corrected. During most days weather conditions were fair requiring only a minor amount of cleaning. However, up to three days caused rather rough conditions and the COOK entrained air bubbles below the ships hull, causing rather noisy data – for example during the time the seismic grid 500 was shot. In total, over 5000-line kilometres of EM122 swath bathymetry were collected during transits, seismic lines and in dedicated surveys to define coring and heat flow sites. Fig. 3.8 provides the full swath coverage obtained during leg 1.

6.1.2 AUV mapping

Initially up to six AUV dives were intended for high-resolution seafloor mapping and visualization. One dive had to be canceled because of delays in port logistics resulting in delayed mobilization of the instrument. A second dive fell victim to adverse sea state. The first attempt was unsuccessful because of buoyancy issues preventing the vehicle form diving. The problems with the trimming of the vehicle persisted during the second attempt, prompting the immediate recovery of the AUV. Unfortunately, the vehicle was severely damaged during the recovery, and was not longer operational, leaving cruise JC228 without high-resolution near-seabed bathymetry data.

6.2 Ocean Bottom refraction seismology

Ocean-Bottom-seismometers were deployed in three deployments. First, we deployed 12 OBS along line P100 in the ODP site 1256 area. The second deployment was in the western portion of the main transect P200 (in-line), including the cross-line P300. The third and last deployment covered the eastern portion of P200, including the cross-line P400 as well as the trench-outer rise of the Nicaraguan/Costa Rican deep-sea trench and subduction zone. In total 96 OBS were deployed; all OBS provided data of very good to excellent quality.

6.2.1 Site 1256 area, P100

Along P100, we deployed 12 OBS (Fig. 6.2.1) and the line was shot at 60 s shot-interval or appox. 150 m. The line aimed to obtain the crustal and upper mantle structure across the ODP site 1256 drilling though the basal/gabbro or layer2/3 boundary of the oceanic crust. Seismic data are of excellent quality, showing a reasonable simple structure with little variations in the OBS record sections. Fig. 6.2.2 provides a data example, revealing (i) a strong crustal phase Pg, turning in upper layer 2 and the lower crust; (ii) a clearly and well-develop wide-angle reflection of PmP branch; (iii) a Pn arrivals, turning in the uppermost mantle. The apparent velocity of Pn is ~7.8-8.0 km/s.

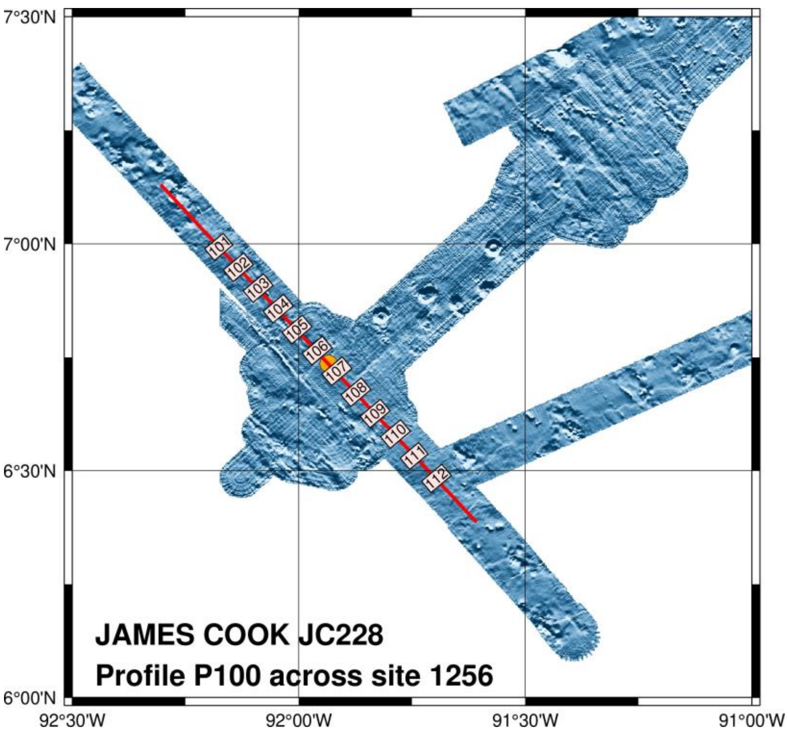

Fig. 6.2.1: Layout of seismic refraction and wide-angle profile P100.

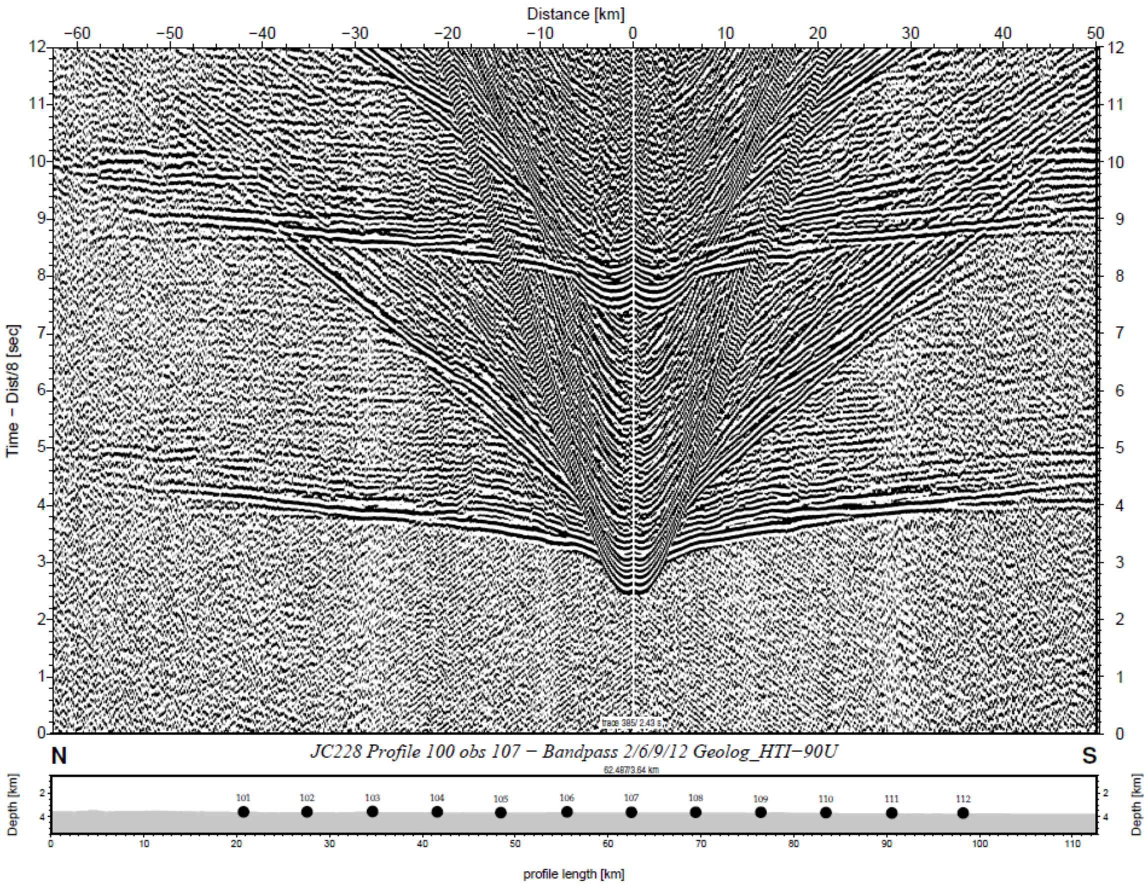

Fig. 6.2.2: Record section from P100, OBS107

6.2.2 Western domain of main survey corridor P200 and P300

Along the western section of P200, we deployed 42 OBS (OBS201-OBS242) and ten additional OBS along P300. OBS were deployed during 12th and 13th of December and OBS201 to OBS222 as well as OBS301 to OBS310 were recovered on the 22nd and 23rd of December. The remaining OBS were left on the seabed to record shots fired in the western and eastern domain and were recovered in early January of 2023. In Figure 6.2.3 stations labelled in green recorded only shots from the shooting in the west, while stations labelled in white stood on the seabed for up to 3 weeks. Figure 6.2.4 shows a sonogram of the time series revealing times of seismic shooting and quite periods during deployment/recovery and when RRS JAMES COOK was engaged elsewhere.

Example record sections are shown in Figures 6.2.5 to 6.2.7 providing shots fired every 60 s (150 m) along P200, 75 m along P200_MCS, and 75 m along P300. Please note the fast Pn along P200 which is basically absent from P300, indicating a strong degree of anisotropy in the upper mantle.

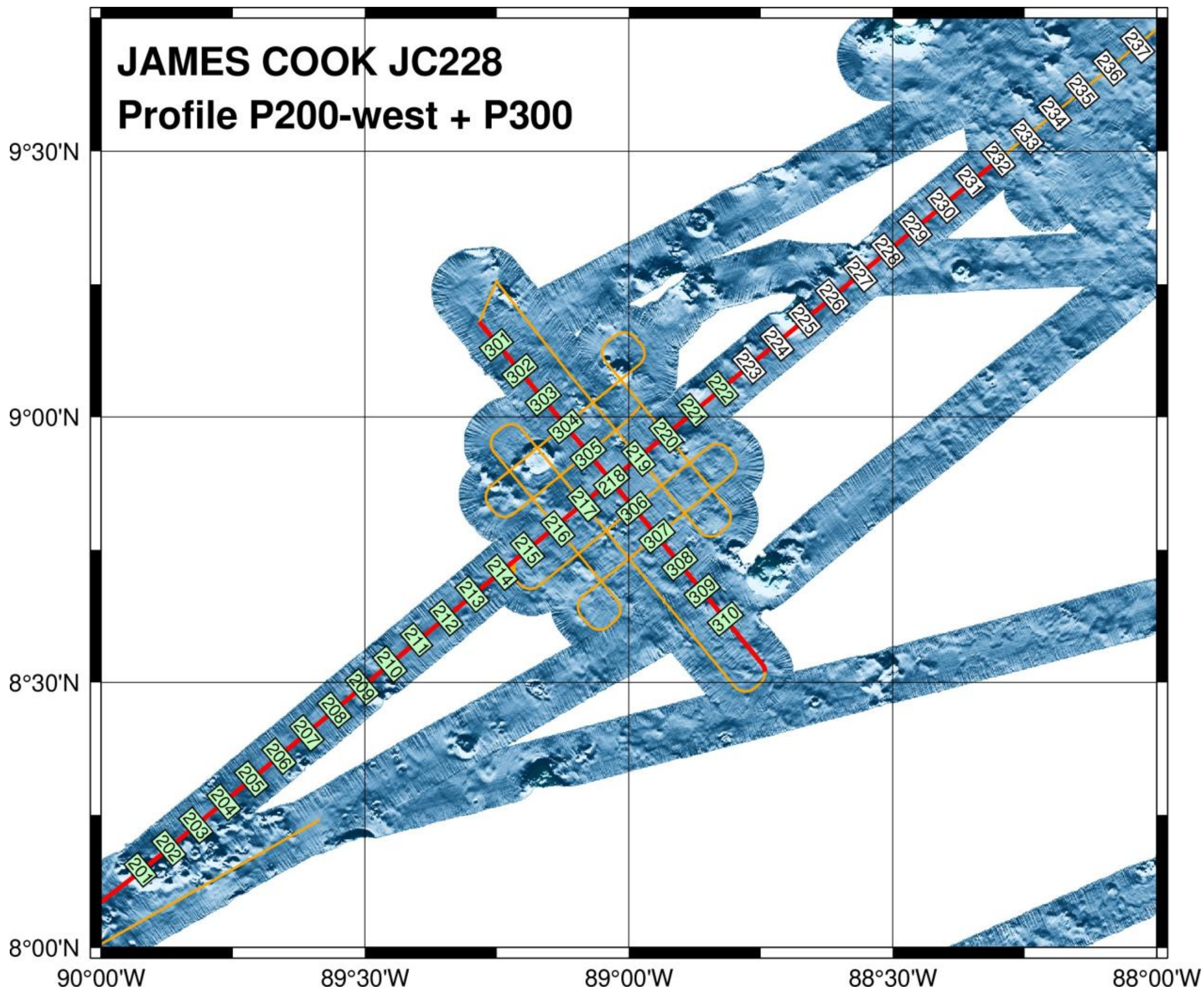

Fig. 6.2.3: Layout of the western section of P200, main tectonic corridor; green OBS deployed between 12.-23.12.22 to record short fired in the western domain only; white: OBS recording shots over 3 weeks. Swath coverage from JC228A; red line: 2D wide-angle; orange: MCS shooting.

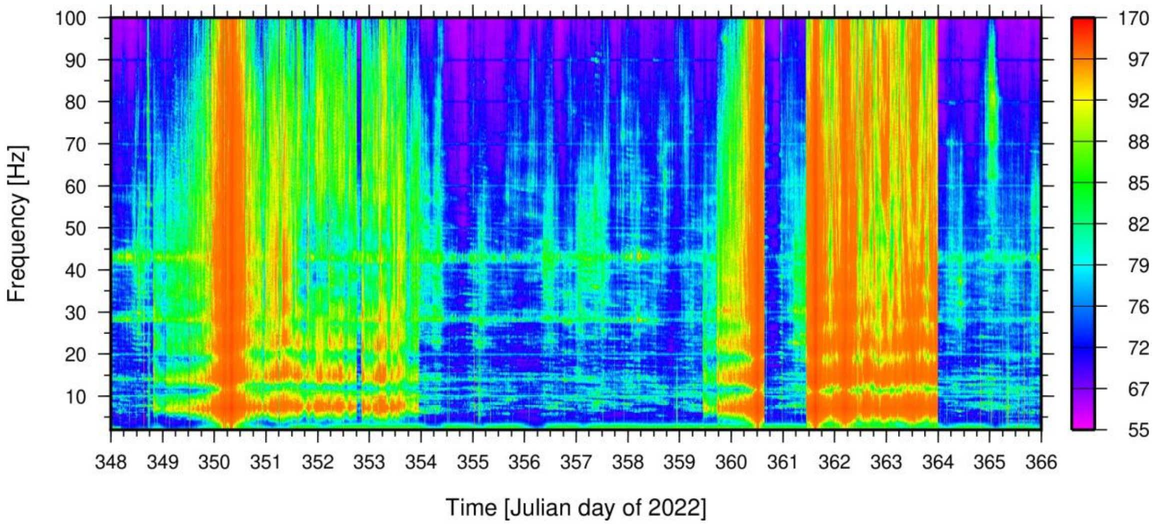

Fig. 6.2.4: Sonogram from OBS232 recoding acoustic sleuths over 18 days.

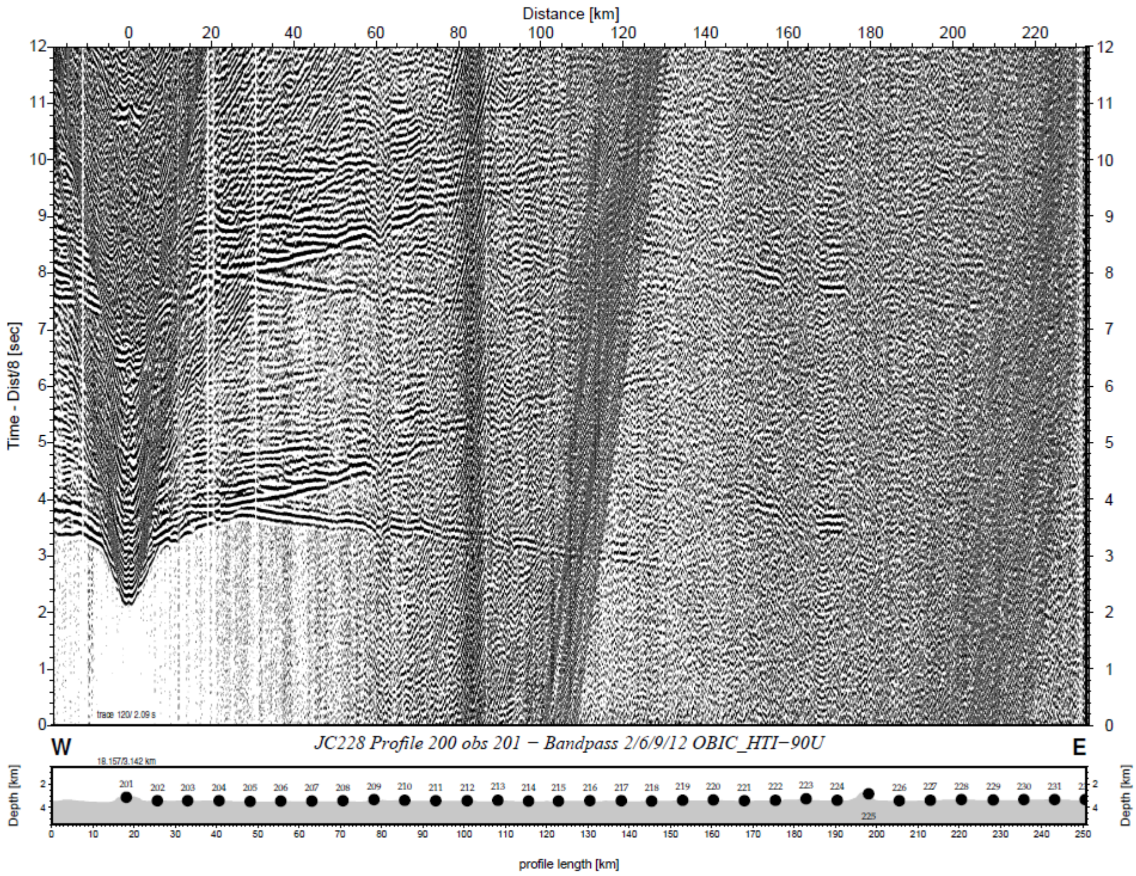

Fig. 6.2.5: Record section from P200w, OBS201 recording shots fired every 60 s (~150 m).

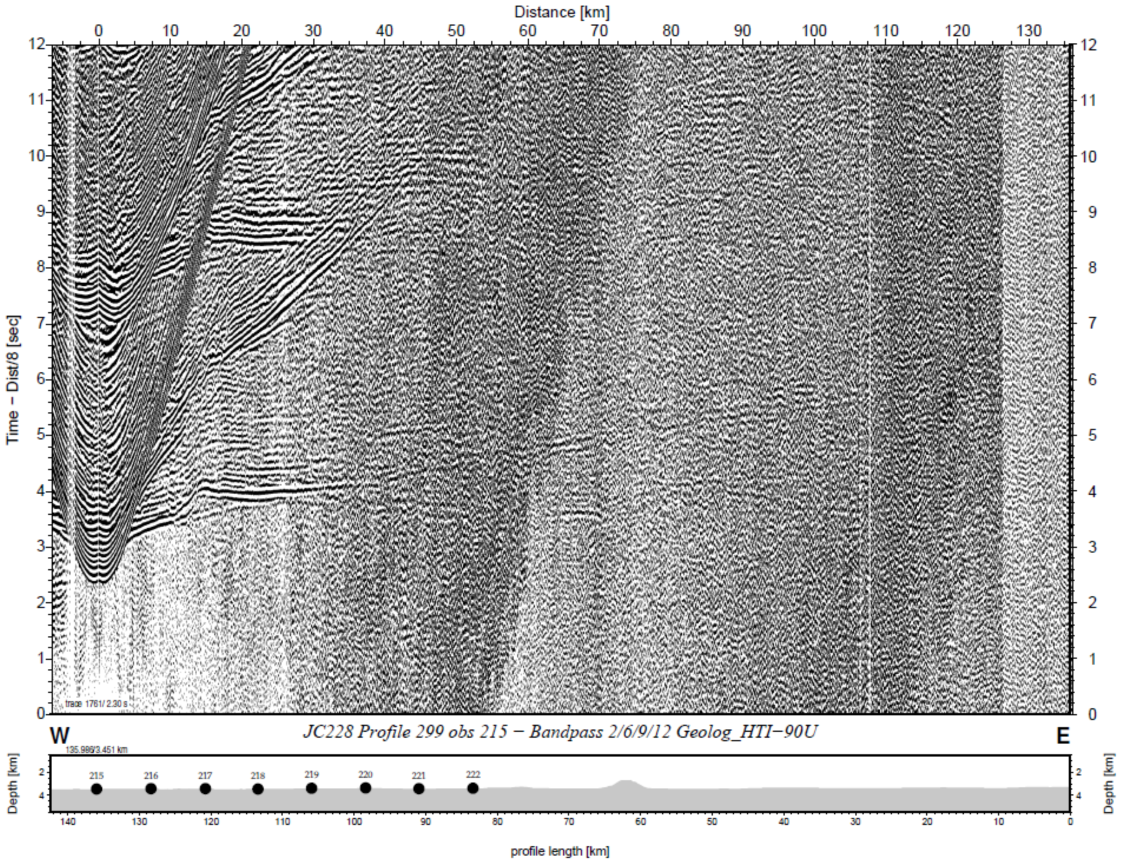

Fig. 6.2.6: Record section from P200w, OBS215 recording shots fired every for MCS at 75 m.

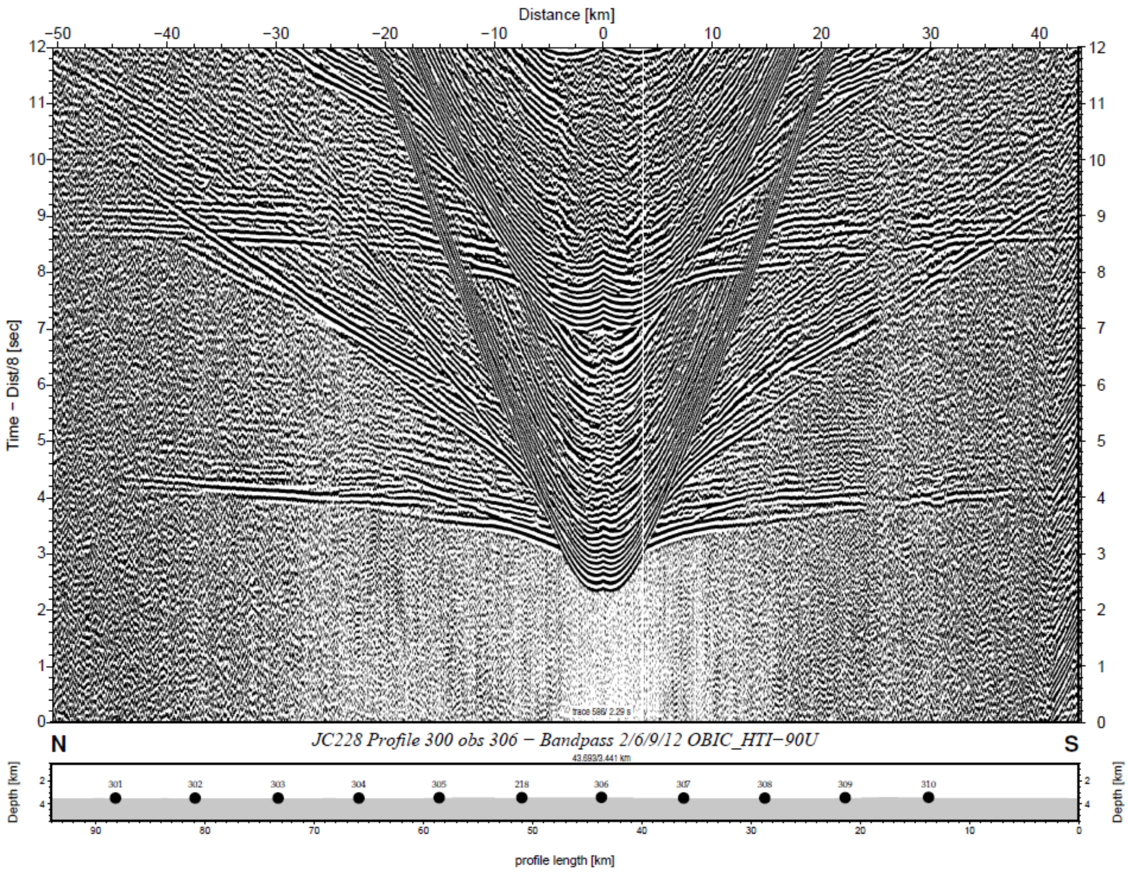

Fig. 6.2.7: Record section from P300, OBS306 recording shots fired every 75 m.

6.2.3 Eastern domain of the main survey corridor P200 and P400

Along the eastern section of P200, we deployed 22 additional OBS (OBS243-OBS264) and ten OBS along P400 (Fig. 6.2.8). In addition, OBS223 to OBS242 from the second deployment also recorded shots fired along the eastern domains and into the deep-sea trench, providing a roughly 400 km long main transect; please not that each line was between 240-250 long, but were shot with some overlap. Again, record sections show very similar features as observed along the previous shooting, but waveforms got more complex in the trench-outer rise area. Interestingly, also record sections along P400 showed a higher degree of complexity when compared with P300, though structure remained reasonable simple.

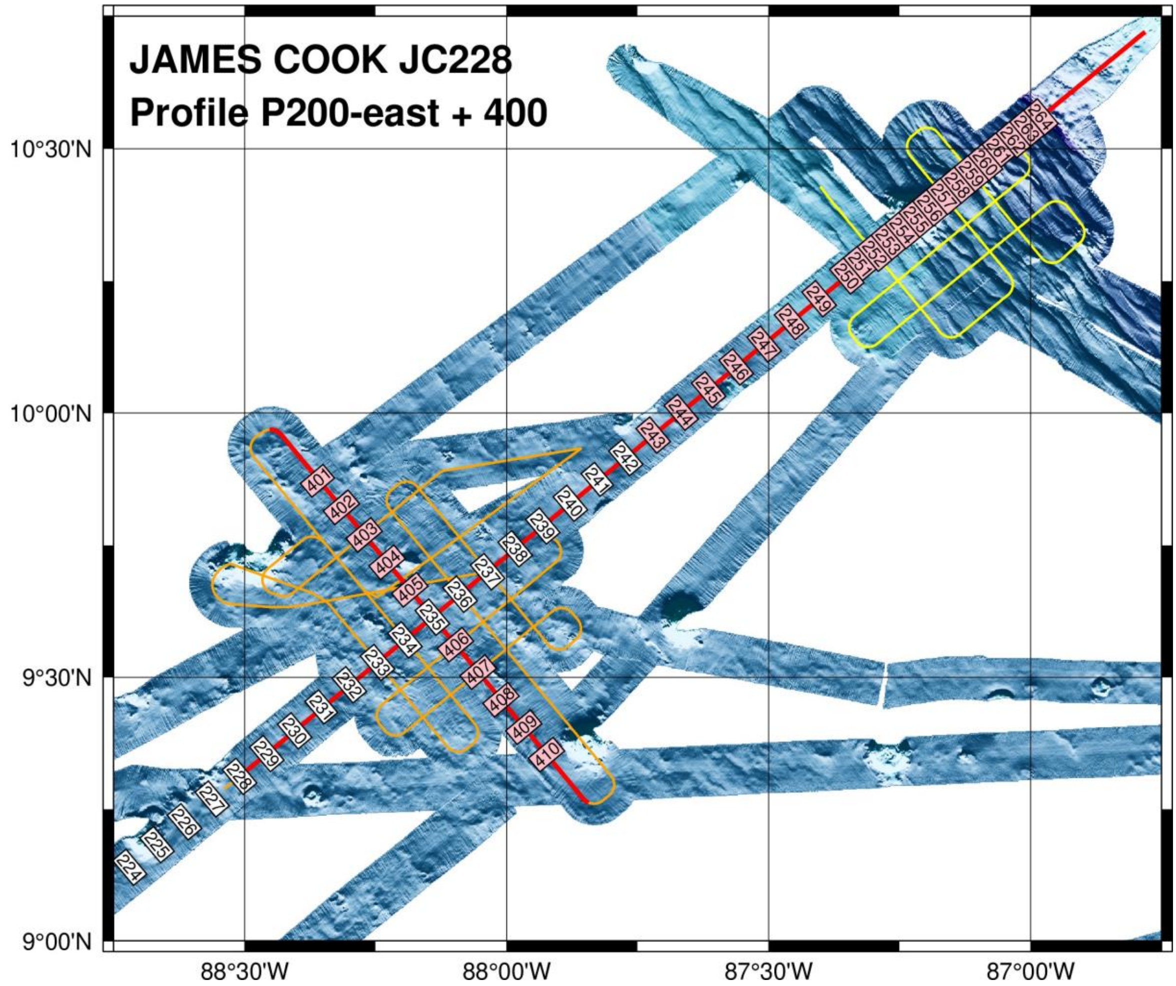

Fig. 6.2.8: Layout of the eastern section of P200, main tectonic corridor and trench-outer rise area; red OBS deployed between 24.12.22 to early January 2023 to record short fired in the eastern domain only; white: OBS recording shots over 3 weeks from both shooting intervals. Swath coverage from JC228A; red line: 2D wide-angle; orange: MCS shooting.

We like to discuss briefly the observed record sections with respect to the aims and the desired features to yield a potential MoHole drill site. The OBS clearly provide very clear crustal arrivals and basically all OBS show a clearly developed and prominent wide-angle Moho reflection, i.e., PmP. Sometimes its features vary with offset or in amplitude, indicating some moderate changes in crustal thickness. Furthermore, differences in Pn character between in-lines and cross-lines clearly support a strongly anisotropic mantle.

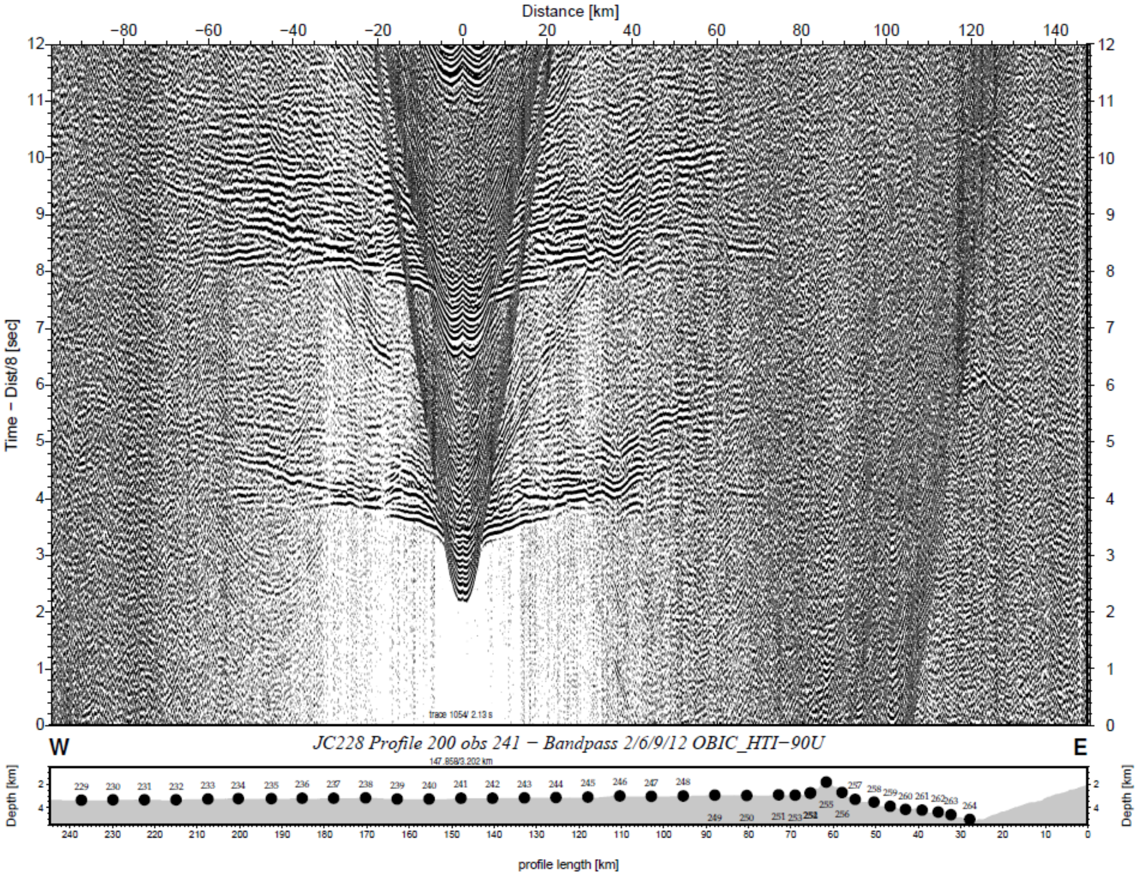

Fig. 6.2.9: Record section from P200e, OBS241 recording shots fired at 60 s.

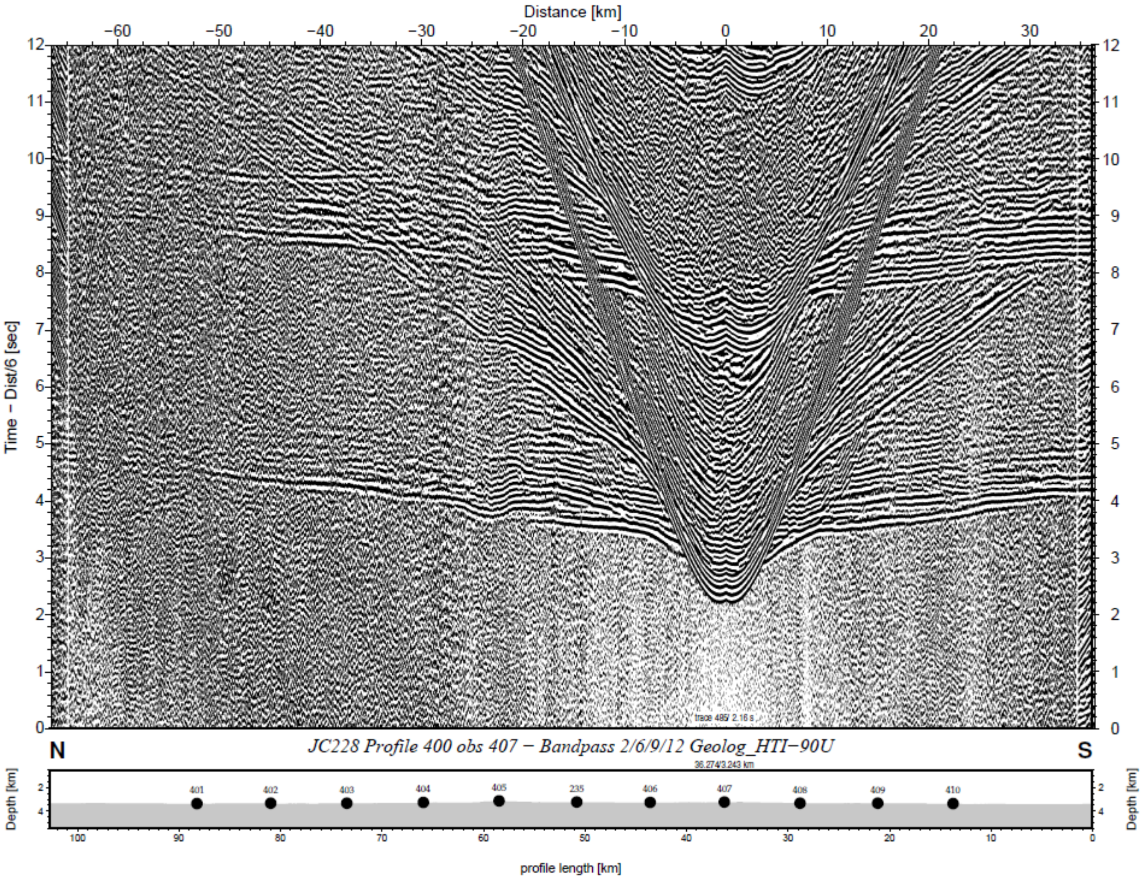

Fig. 6.2.10: Record section from P400, OBS407 recording shots fired every 75 m.

6.3 Multi-channel seismic data imaging

Seismic reflection data were processed on board the vessel using Landmark SeisSpace version 5000.11.0. Geometry for each line was assigned using the SEG-P1 files generated from the Triggerfish navigation system, which give the calculated position of the source and each streamer group at every shot time. A 6.25 m common midpoint (CMP) interval was used, based on line azimuths of either 051° or 321°, so that CMP numbers increase consistently to the NE for flowline profiles and to the NW for isochron profiles. Several profiles were acquired in sections due to problems with the different acquisition computers or due to on-board emergencies, and they were merged at this stage. Statics were applied to sea level based on a source depth of 9 m and a streamer depth of 12 m. Two SEGY files were written for each profile. The first contains only the auxiliary channels for each shot (the trigger to the Bigshot, water break hydrophone, and the hydrophones mounted on the airgun beams). The second contains the data channels with the geometry applied, but no additional processing, which should be immediately usable for import into different processing flows. The start of the multichannel seismic records is 150 ms before the shot instant.

On-board processing was focused initially on quality control. This included checking that the offset between the source and active streamer was correct based on the water wave arrival time on the water break hydrophone and channel 1. Data to be processed were bandpass filtered and resampled to 4 ms. A static shift of -150 ms was applied. Predictive deconvolution was applied using parameters selected by a combination of examining the autocorrelation of the traces and testing a range of parameters to derive a compact wavelet without losing low frequency content needed for the crustal imaging. True amplitude recovery used a time to power gain function. Trace mixing across the streamer groups was applied before sorting into CMP gathers. Velocity analysis was carried out at ~5 km spacing along the profiles using semblance, constant velocity stacks, and ensuring flattening of reflections within the CMP gathers. The density of velocity picks was increased in regions where there was significant basement topography, otherwise there was little evidence in the data to require changes in the stacking velocities. If there were no clear events beneath the top of oceanic basement, velocities were assigned based on an expected oceanic crustal interval velocity structure. Normal moveout correction was applied before stacking. The first seabed multiple is significantly later than the expected base of the crust, so no multiple suppression was applied.

The stacked sections show strong reflections from the seabed and sedimentary section. The sediments have a typical thickness in two-way time of 400-500 ms, and form laterally continuous packages. Based on converting the picked stacking velocities into interval velocity, this corresponds to 300-400 m. Approaching the trench the seabed becomes heavily faulted with at least some of the faults eventually having a larger offset than the sediment thickness. There are some signs that individual sediment packages vary in their thickness over distances of 10s of km indicating that there is minor long-wavelength plate deformation away from the subduction zone.

The top of the oceanic basement is shown as a strong, uneven, highly scattering surface. In addition to the seamounts that are visible on the swath bathymetry, there are numerous less high seamounts that do not break the seabed. Beneath the seabed variable reflections can be seen, including dipping events and flat-lying events. We interpret a regionally extensive, but nevertheless variable, reflection that is typically ~1700-1800 ms beneath the top of the oceanic basement as being the near-normal incidence Moho reflection. Locally this is sufficiently strong to be identified within the unstacked CMP gathers.

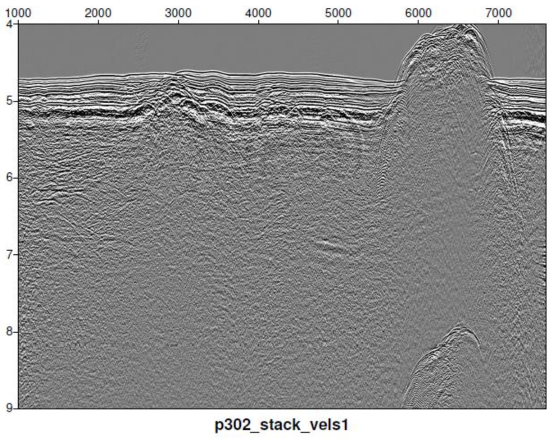

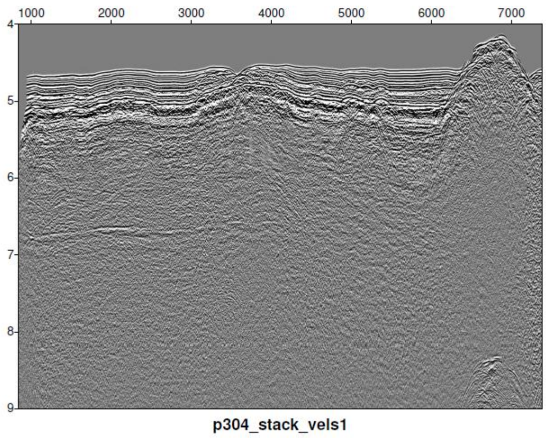

Fig. 6.3.1: Example of onboard processes seismic profiles in the grid-300 area.

Due to the strong scattering from the top of basement we also carried out some experiments with migration. Post-stack Kirchhoff water-velocity migration was effective at collapsing most of the diffractions from the top of basement but needed a tail mute to remove the seabed multiple energy. Pre-stack Kirchhoff migration using the stacking velocities was more effective at producing high-quality images even though this was more computationally intensive and there was insufficient time to refine the velocity models based on the migrated offset sections.

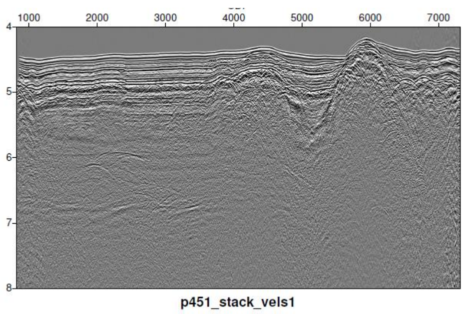

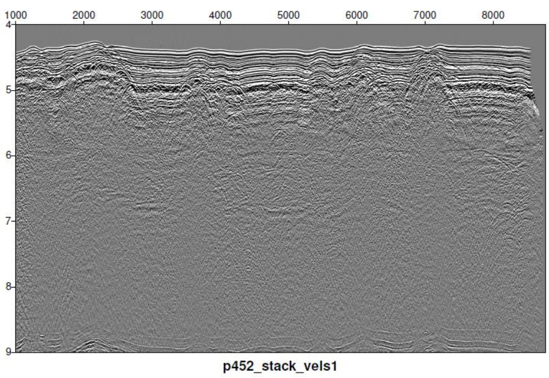

Fig. 6.3.2: Example of onboard processes seismic profiles in the grid-400 area.

The MCS data acquired during JC228 seem to fulfil most of the “desired” criteria for MoHole drilling and hence show a seismic reflection Moho, though it’s in places discontinuous and not as prominent as the wide-angle Moho described in chapter 6.2.

6.4 Heat flow measurements

A total number of 66 geothermal gradient measurements (example is shown in Figure 6.4.1) were obtained at 9 stations (Fig. 6.4.2), of which 64 sites gave reliable results, corresponding to a success rate of 97 %. The sediments allowed full penetration depth in most cases and we find little or no transient temperature disturbances; thus, bottom water currents appear to be low or absent.

Core	Mean t_c [W/mK]
GC1	0,708
GC2	0,699
GC3	0,698
GC4	0,713
GC5	0,706
GC6	-
GC7	0,716
GC8	0,717
GC9	0,839
GC10	0,695
GC11	0,687
GC12	-
GC13	-
GC14	0,713
GC15	0,695
GC16	0,684

Tab. 6.4.1: Mean thermal conductivity values.

The area west of Costa Rica into the Guatemala Basin is characterized by geothermally “hot” and ”cold” areas (Hutnak et al., 2008). “Hot” and ”cold” in this case refers to the expected heat flow value of 110 mW/m^2 for a crustal age of 20 Ma. The varying geometry of bending-related faults in the outer rise from simple shear faults to antithetic faults might be correlated to different processes of fluid flow along the faults. We examined a section of the supposed bend-fault system at sites from 10° 24’N to 9° 45’N some 40 Nm SE of a pronounced seamount. This includes the transition from the “cold” area with heat flow values of 10–20 mW/m^2 to the “hot” area, where heat flow values of 150–200 mWm^2 are abundant.

Thermal conductivity values were measured on whole round cores and values are fairly homogenous throughout the area (Fig. 6.4.3., Table 6.4.1) with little increase with depth. Mean values range from 0.69 to 0.72 W/mK. These values correspond well to a muddy, water rich sediment of pelagic sedimentation.

We find that all sites north of 9°55’N belong to the “cold” regime, while all sites south of 9°55’N are classified as “hot” (Fig. 6.4.4; Fig. 6.4.5).

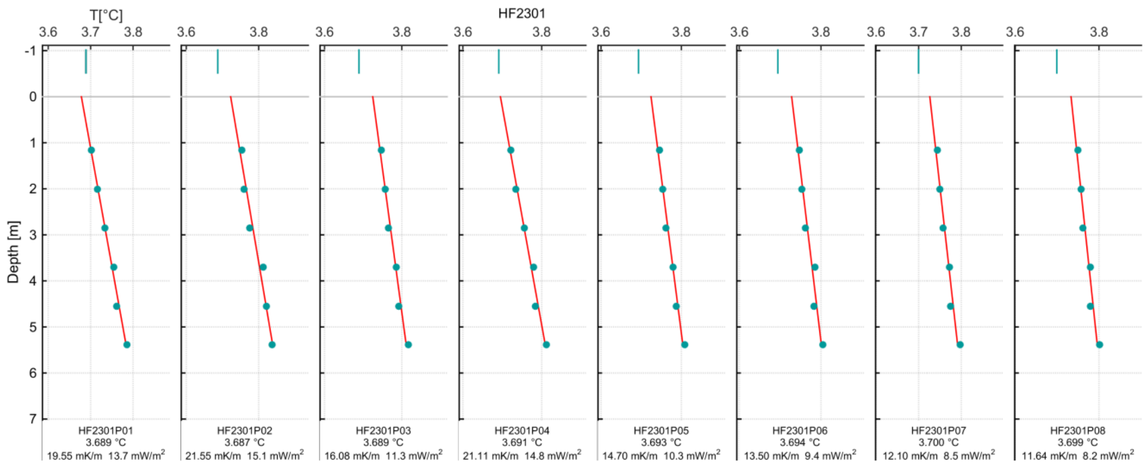

Fig. 6.4.1 Station HF2301 comprising 8 individual sites. A penetration depth of 6 m occurs regularly in the area.

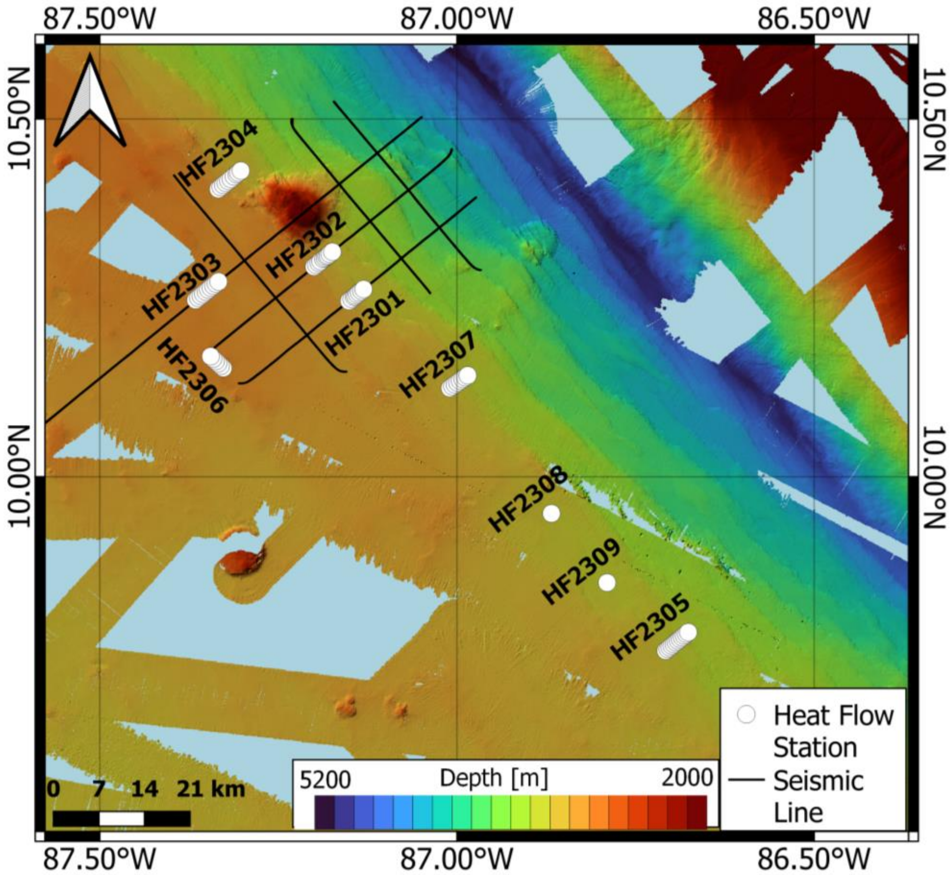

Fig. 6.4.2: Locations of HF stations HF2301 – HF2309 along the presumed bend faults.

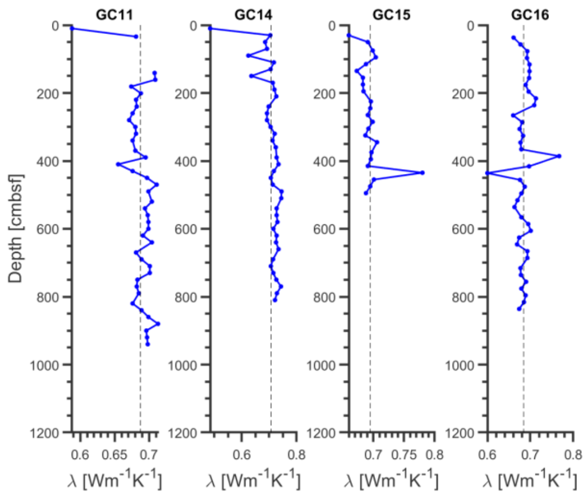

Fig. 6.4.3 Example of thermal conductivity measurements on long cores.

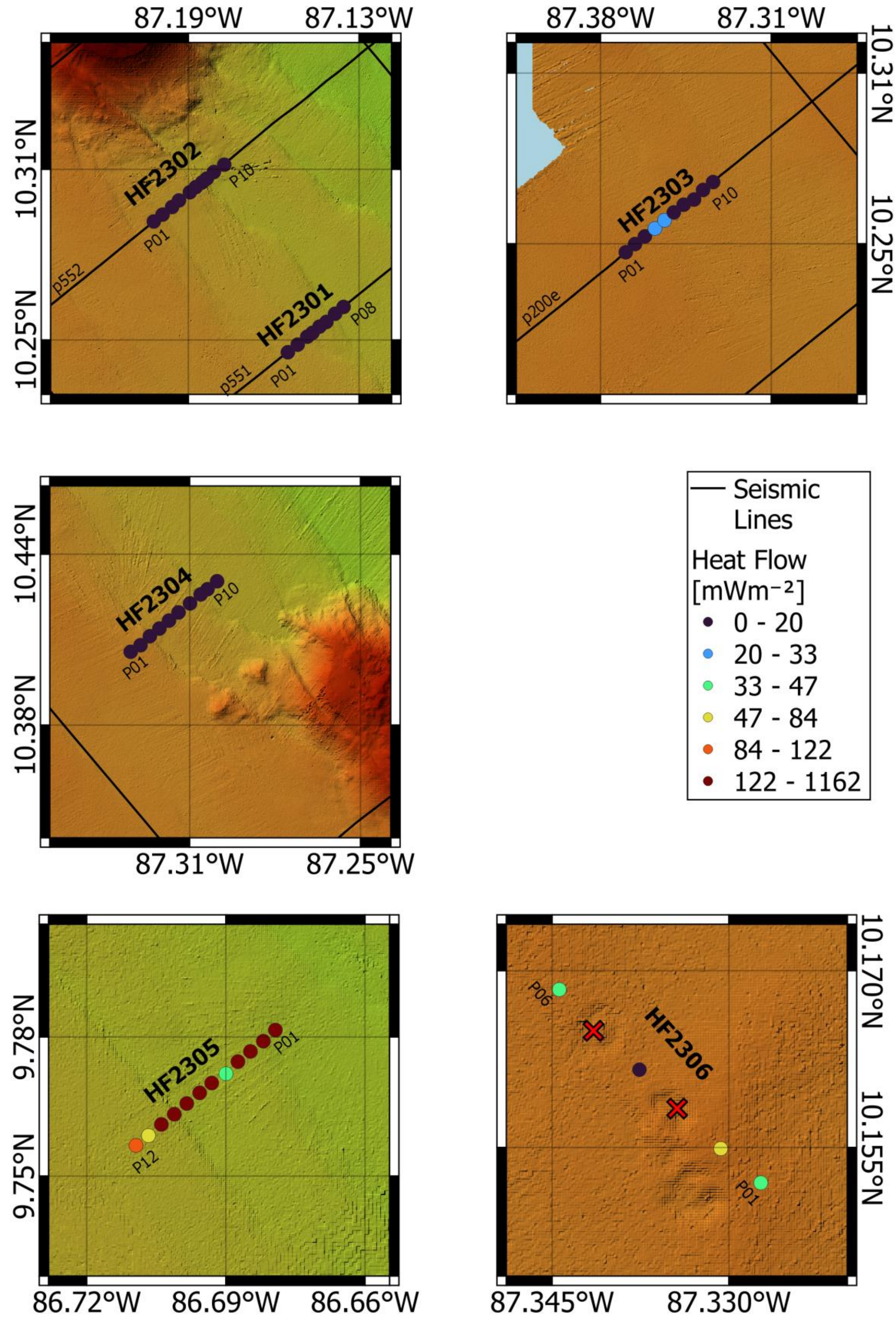

Fig. 6.4.4: Preliminary results of the individual stations. The trials on two circular structures on station HF2306 failed completely due to hard ground.

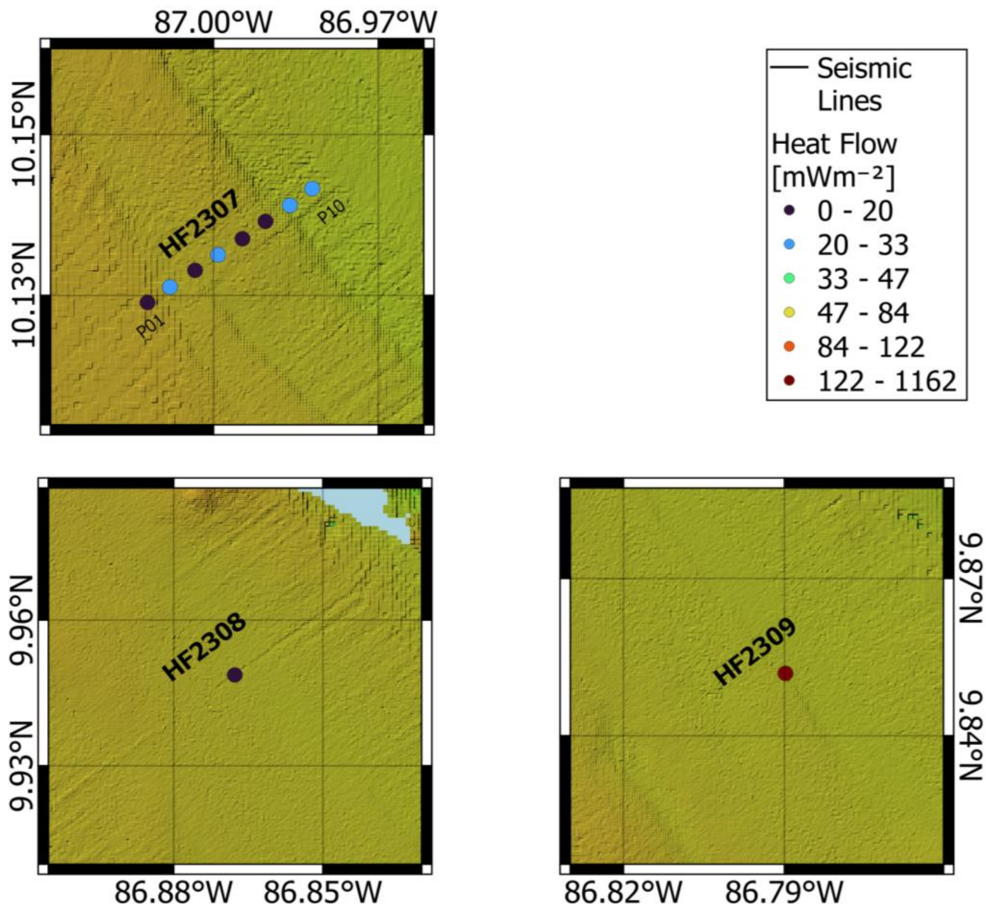

Fig. 6.4.5: Heat flow stations HF2307 – HF2309. Stations 8 and 9 are collocated with gravity corers GC15 and GC16.

6.5 Coring and pore water

During JC228A a total of 16 gravity cores were taken utilising several different core barrel lengths, for details see Table 7.6. Following recovery, the cores were sectioned in to maximum 1.5m lengths, the cores were identified/named from bottom to top. The cores were not split on board but kept as whole rounds. The core sections were moved to the deck lab and for thermal conductivity measurements and pore fluid extraction. Following this the cores were transferred to a 4°C refrigerated container for storage until their return to Southampton with the vessel.

Following the thermal conductivity analysis, pore fluids were extracted using rhizomes. The water samples had their pH measured, using 0-14 pH indicator strips, before being sub divided for future shore-based analysis. Two splits were taken an unacidified split for anion analysis and a split acidified with concentrated nitric acid (Romil UpA) for cation analysis. The number of samples taken for each core are given in Table 7.6.

6.6 Magnetic measurements of spreading anomalies

During JC228A a magnetometer was towed during all seismic operations and along some major transits, with a small number of additional profiles collected during rough seas during JC228B. In total, 4580 km of magnetic data was acquired. A survey in close proximity to the magnetic equator may cause poor magnetic seafloor spreading anomalies. However, throughout the area clear spreading anomalies were observed and can often being well correlated between profiles. Later, in a post-cruise data analysis, we will be able to define seafloor ages based on true magnetic anomalies instead of the current interpolated models. Figure 6.6.1 shows the observed magnetic anomaly pattern colour coded by amplitude.

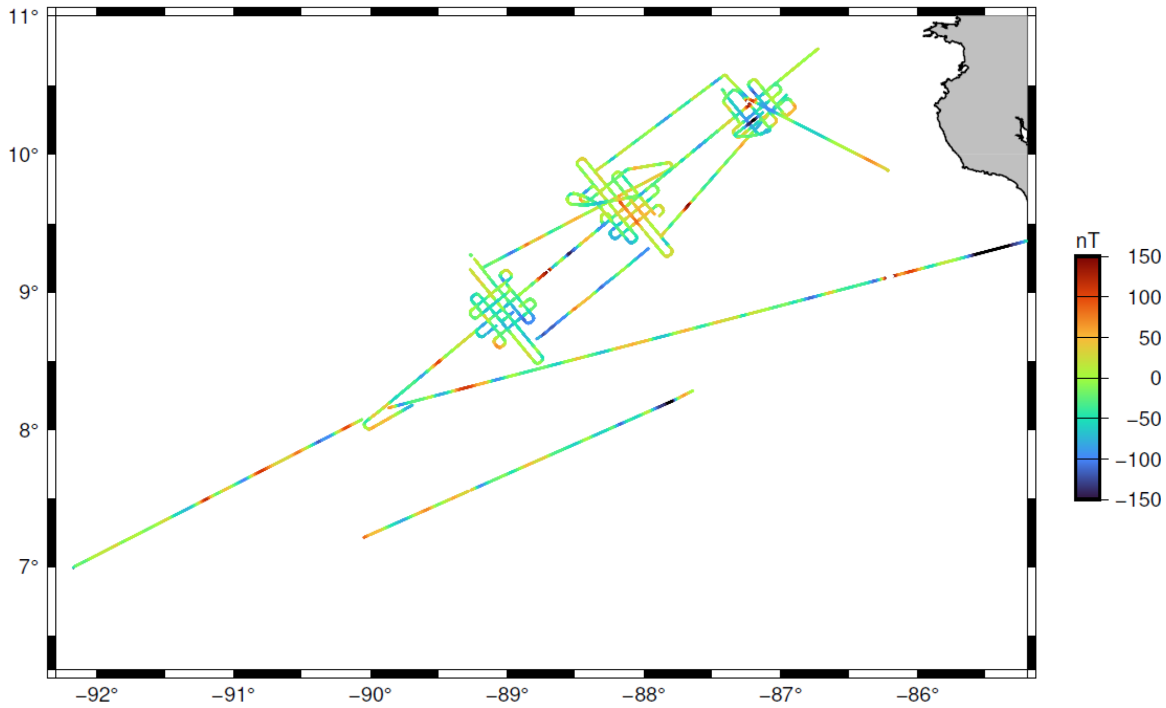

Fig. 6.6.1: Magnetic seafloor spreading reversals recorded in the survey area.

7 Station List JC228

7.1 Station Lists of Ocean-Bottom-Seismometer deployments and seismic lines, leg 1

Station No.		Date	Gear	Date	Latitude	Longitude	Water Depth	Remarks / clock drift
COOK	SciParty	deploy	OBS	recover	[°N]	[°W]	[m]	[ms]
JC228-OBS101	OBS101	09.12.22	GEOMAR	11.12.22	6°59.53	92°10.52	3587	-1,86
JC228-OBS102	OBS102	09.12.22	GEOMAR	11.12.22	6°56.77	92°07.91	3601	0,38
JC228-OBS103	OBS103	09.12.22	GEOMAR	11.12.22	6°54.01	92°05.33	3584	6,63
JC228-OBS104	OBS104	09.12.22	GEOMAR	11.12.22	6°51.24	92°02.78	3617	0,36
JC228-OBS105	OBS105	09.12.22	GEOMAR	11.12.22	6°48.47	92°00.17	3657	0,36
JC228-OBS106	OBS106	09.12.22	GEOMAR	11.12.22	6°45.70	91°57.59	3606	-0,31
JC228-OBS107	OBS107	09.12.22	GEOMAR	11.12.22	6°42.93	91°54.96	3640	0,87
JC228-OBS108	OBS108	09.12.22	GEOMAR	11.12.22	6°40.21	91°52.37	3627	1,52
JC228-OBS109	OBS109	09.12.22	GEOMAR	11.12.22	6°37.43	91°49.79	3650	0,22
JC228-OBS110	OBS110	09.12.22	GEOMAR	11.12.22	6°34.71	91°47.20	3679	0,95
JC228-OBS111	OBS111	09.12.22	GEOMAR	11.12.22	6°31.94	91°44.60	3713	4,48
JC228-OBS112	OBS112	09.12.22	GEOMAR	11.12.22	6°29.17	91°42.02	3713	-1,77

Tab. 7.1 OBS deployment No. 1 at ODP site 1256

Station No.		Date	Gear	Date	Latitude	Longitude	Water Depth	Remarks / clock drift
COOK	SciParty	deploy	OBS	recover	[°N]	[°W]	[m]	[ms]
JC228-OBS201	OBS201	12.12.22	OBIC	22.12.22	8°8.694	89°55.4	3145	-47.55
JC228-OBS202	OBS202	12.12.22	OBIC	22.12.22	8°11.2924	89°52.2575	3431	-5.32
JC228-OBS203	OBS203	12.12.22	OBIC	22.12.22	8°13.9039	89°49.1663	3451	-16.06
JC228-OBS204	OBS204	12.12.22	OBIC	22.12.22	8°16.4796	89°45.9974	3446	-24.19
JC228-OBS205	OBS205	12.12.22	OBIC	22.12.22	8°19.0835	89°42.8707	3502	-5.39
JC228-OBS206	OBS206	12.12.22	OBIC	22.12.22	8°21.6773	89°39.7366	3468	-35.59
JC228-OBS207	OBS207	12.12.22	OBIC	22.12.22	8°24.2476	89°36.5854	3472	-218.81
JC228-OBS208	OBS208	12.12.22	OBIC	22.12.22	8°26.8529	89°33.4707	3462	78.48
JC228-OBS209	OBS209	12.12.22	OBIC	22.12.22	8°229.4415	89°30.3091	3314	60.34
JC228-OBS210	OBS 210	12.12.22	GEOMAR	22.12.22	8°32,02110	89°27,20160	3419	-8,53
JC228-OBS211	OBS 211	12.12.22	GEOMAR	22.12.22	8°34,64982	89°24,09186	3430	1,89
JC228-OBS212	OBS 212	12.12.22	GEOMAR	22.12.22	8°37,25244	89°20,86848	3447	4,91
JC228-OBS213	OBS 213	12.12.22	GEOMAR	22.12.22	8°39,98848	89°17,78460	3401	1,96
JC228-OBS214	OBS 214	12.12.22	GEOMAR	22.12.22	8°42,44178	89°14,58630	3476	-1,22
JC228-OBS215	OBS 215	12.12.22	GEOMAR	22.12.22	8°45,01092	89°11,49720	3461	37,25
JC228-OBS216	OBS 216	12.12.22	GEOMAR	22.12.22	8°47,62872	89°8,34456	3455	31,27
JC228-OBS217	OBS 217	13.12.22	GEOMAR	22.12.22	8°50,230	89°05,180	3452	-10,34
JC228-OBS218	OBS 218	13.12.22	GEOMAR	22.12.22	8°52,79094	89°2,04174	3464	13,07
JC228-OBS219	OBS 219	13.12.22	GEOMAR	22.12.22	8°55,40346	88°58,92534	3419	8,75
JC228-OBS220	OBS 220	13.12.22	GEOMAR	23.12.22	8°57,98742	88°55,77900	3375	15,47
JC228-OBS221	OBS 221	13.12.22	GEOMAR	23.12.22	9°0,57150	88°52,64520	3456	2,04
JC228-OBS222	OBS222	13.12.22	OBIC	23.12.22	9°3.18108	88° 49.4863	3419	-105.294
JC228-OBS223	OBS223	13.12.22	OBIC	01.01.23	9°5.76582	88° 46.3407	3274	-10.6872
JC228-OBS224	OBS224	13.12.22	OBIC	01.01.23	9°8.35512	88° 43.1767	3408	-85.061
JC228-OBS225	OBS225	13.12.22	OBIC	01.01.23	9°10.9921	88°40.0079	3214	1.6478
JC228-OBS226	OBS226	13.12.22	OBIC	02.01.23	9°13.5835	88°36.855	3441	40.6736
JC228-OBS227	OBS227	13.12.22	OBIC	02.01.23	9°16.165	88°33.6941	3424	25.0261
JC228-OBS228	OBS228	13.12.22	OBIC	02.01.23	9°18.7446	88°30.5926	3351	-26.5409
JC228-OBS229	OBS 229	13.12.22	GEOMAR	01.01.23	9°21,31752	88°27,43612	3381	26,39
JC228-OBS230	OBS 230	13.12.22	GEOMAR	01.01.23	9°23,91132	88°24,25230	3356	49,41
JC228-OBS231	OBS 231	13.12.22	GEOMAR	01.01.23	9°26,50782	88°21,10842	3335	45,17
JC228-OBS232	OBS 232	13.12.22	GEOMAR	02.01.23	9°29,13966	88°17,98464	3359	16,88
JC228-OBS233	OBS 233	13.12.22	GEOMAR	02.01.23	9°31,66854	88°14,75952	3280	3,12
JC228-OBS234	OBS234	13.12.22	OBIC	07.01.23	9°34.2668	88°11.6682	3351	-199.937
JC228-OBS235	OBS235	13.12.22	OBIC	01.01.23	9°36.9227	88°8.49474	3249	124.125

Tab. 7.2.1 OBS deployment No. 2 of western-segment of P200 and grid 300 with P300

Station No.		Date	Gear	Date	Latitude	Longitude	Water Depth	Remarks / clock drift
COOK	SciParty	deploy	OBS	recover	[°N]	[°W]	[m]	[ms]
JC228-OBS236	OBS236	13.12.22	OBIC	07.01.23	9°39.4666	88°5.28066	3241	-147.64
JC228-OBS237	OBS237	13.12.22	OBIC	07.01.23	9°42.0458	88°2.18802	3228	-25.1315
JC228-OBS238	OBS238	13.12.22	OBIC	07.01.23	9°44.5694	87°58.9953	3219	16.1952
JC228-OBS239	OBS239	13.12.22	OBIC	07.01.23	9°47.1429	87°55.8227	3192	-43.1377
JC228-OBS240	OBS240	13.12.22	OBIC	07.01.23	9°49.7212	87°52.6972	3263	-280.392
JC228-OBS241	OBS241	13.12.22	OBIC	07.01.23	9°52.3097	87°49.5172	3292	-28.8344
JC228-OBS242	OBS242	13.12.22	OBIC	07.01.23	9°54.9695	87°46.347	3221	96.8048
JC228-OBS301	OBS 301	13.12.22	GEOMAR	23.12.22	9°8,40930	89°15,07230	3497,7	-3,5
JC228-OBS302	OBS 302	13.12.22	GEOMAR	23.12.22	9°5,33532	89°12,48846	3499,6	35,32
JC228-OBS303	OBS 303	13.12.22	GEOMAR	23.12.22	9°02,19774	89°09,84198	3508	1,6
JC228-OBS304	OBS 304	14.12.22	GEOMAR	23.12.22	8°59,05266	89°7,30500	3510,7	14,5
JC228-OBS305	OBS 305	14.12.22	GEOMAR	23.12.22	8°55,93788	89°4,68228	3481,8	46,14
JC228-OBS306	OBS306	14.12.22	OBIC	23.12.22	8°49.7125	88°59.4664	3452	-1.0174
JC228-OBS307	OBS307	14.12.22	OBIC	23.12.22	8°46.5463	88°56.8703	3503	48.525
JC228-OBS308	OBS308	14.12.22	OBIC	23.12.22	8°43.4284	88°54.2244	3522	-0.0681
JC228-OBS309	OBS309	14.12.22	OBIC	23.12.22	8°40.3427	88°51.6531	3480	-80.4742
JC228-OBS310	OBS310	14.12.22	OBIC	23.12.22	8°37.2008	88°49.0219	3427	-128.321

Tab. 7.2.2 OBS deployment No. 2 of western-segment of P200 and grid 300 with P300, continued

Station No.		Date	Gear	Date	Latitude	Longitude	Water Depth	Remarks / clock drift
COOK	SciParty	deploy	OBS	recover	[°N]	[°W]	[m]	[ms]
JC228-OBS243	OBS243	24.12.22	OBIC	07.01.23	9° 57.554	8739.9842	3160	-7.90
JC228-OBS244	OBS244	24.12.22	OBIC	07.01.23	10° 0.105	87°36.8872	3146	-34.10
JC228-OBS245	OBS245	24.12.22	OBIC	07.01.23	10°2.64228	87°33.6973	3118	-189.48
JC228-OBS246	OBS246	24.12.22	OBIC	06.01.23	10°5.23254	87°30.5312	3020	-68.09
JC228-OBS247	OBS247	24.12.22	OBIC	06.01.23	10°7.80864	87°27.369	3036	-112.53
JC228-OBS248	OBS248	24.12.22	OBIC	06.01.23	10°10.3835	87°24.2096	3016	-21.13
JC228-OBS249	OBS249	24.12.22	OBIC	06.01.23	10°12.9784	87°21.0428	2944	2.85
JC228-OBS250	OBS250	24.12.22	OBIC	06.01.23	10°15.5559	87°19.4354	2960	-7.95
JC228-OBS251	OBS251	24.12.22	OBIC	06.01.23	10°16.8353	87°17.8792	2975	1.25
JC228-OBS252	OBS252	24.12.22	OBIC	06.01.23	10°18.1456	88°59.4664	2925	72.13
JC228-OBS253	OBS 253	24.12.22	GEOMAR	31.12.222	10°19,46166	87°16,24799	2936	5,87
JC228-OBS254	OBS 254	24.12.22	GEOMAR	31.12.222	10°20,69706	87°14,70384	2671	1,39
JC228-OBS255	OBS 255	24.12.22	GEOMAR	31.12.222	10°22,03722	87°13,13010	2150	3,68
JC228-OBS256	OBS 256	24.12.22	GEOMAR	31.12.222	10°23,26902	87°11,53242	2368	1,43
JC228-OBS257	OBS 257	25.12.22	GEOMAR	31.12.222	10°24,37350	87°10,19832	3216	-2,16
JC228-OBS258	OBS 258	25.12.22	GEOMAR	31.12.222	10°25,88994	87°8,34924	3539	26,69
JC228-OBS259	OBS 259	25.12.22	GEOMAR	31.12.222	10°27,17742	87°6,75510	3576	23,02
JC228-OBS260	OBS 260	25.12.22	GEOMAR	31.12.222	10°28,49148	87°5,17266	3938	9,39
JC228-OBS260	OBS 261	25.12.22	GEOMAR	31.12.222	10°29,75238	87°3,55540	4222	11,96
JC228-OBS262	OBS 262	25.12.22	GEOMAR	31.12.222	10°31,02630	87°1,98996	4381	4.,04
JC228-OBS263	OBS 263	25.12.22	GEOMAR	31.12.22	10°32,32614	87°00,46914	4635	8,64
JC228-OBS264	OBS 264	25.12.22	GEOMAR	31.12.22	10°33,55158	86°58,81848	4943	1,56
JC228-OBS401	OBS401	25.12.22	OBIC	01.01.23	9°52.4358	88°21.5337	3357	-52.54
JC228-OBS402	OBS402	25.12.22	OBIC	01.01.23	9°49.3251	88°18.9527	3358	-314.57
JC228-OBS403	OBS403	25.12.22	OBIC	01.01.23	9°46.1986	88°16.3228	3344	119.50
JC228-OBS404	OBS404	25.12.22	OBIC	02.01.23	9°43.0829	88°13.6859	3285	93.60
JC228-OBS405	OBS405	25.12.22	OBIC	02.01.23	9°39.9539	88°11.0769	3138	-145.37
JC228-OBS406	OBS 406	24.12.22	GEOMAR	01.01.23	9°33,71118	88°5,84574	3289	42,07
JC228-OBS407	OBS 407	24.12.22	GEOMAR	01.01.23	9°30,58698	88°3,23682	3250	-7,98
JC228-OBS408	OBS 408	24.12.22	GEOMAR	01.01.23	9°27,47592	88°0,67854	3336	1,39
JC228-OBS409	OBS 409	24.12.22	GEOMAR	01.01.23	9°24,35616	87°58,01772	3343	35,34
JC228-OBS410	OBS 410	24.12.22	GEOMAR	01.01.23	9°21,24168	87°55,46934	3381	-2,95

Tab. 7.3 OBS deployment No. 3 of eastern-segment of P200 and grid 400 with P400

Line name	Long. begin	Lat. begin	Day/time	Long. end	Lat. end	Day/time	Comments
	[°W]	[°N]	[jday/time]	[°W]	[°N]	[jday/time]	
JC228_p100	92.30483	7.130531	344/203700	92.26758	7.09064	344/211400	Profile p100 at ODP site 1246
JC228_p199	89,74826	8,1491	348/221000	90,00189	8,00597	349/015200	Line after deploy streamer & guns
JC228_p199a	90,00442	8,00524	349/015400	90,00709	8,08051	349/032300	Turn onto P200
JC228_p200_OBSW	90,00154	8,08485	349/032800	89,71133	8,32064	349/081200	OBS line from SW end
JC228_p200a	88,30561	9,48633	350/065800	88,30286	9,48158	350/100700	Turn from OBS onto MCS line
JC228_p200_MCSW	88,30749	9,47786	350/101149	89,21525	8,73072	351/005835	MCS line from NE to grid 1
JC228_p352a	89,22079	8,72201	351/010600	89,1735	8,67999	351/020930	Turn from 200 MCS onto 352
JC228_p352	89,17178	8,6811	351/021117	88,85036	8,94265	351/081844	
JC228_p352b	88,83652	8,94911	351/083330	88,80833	8,88958	351/094630	Turn from 352 to 351
JC228_p351	88,81122	8,88719	351/094921	89,08778	8,66205	351/141308	
JC228_p351a	89,09157	8,65771	351/141730	89,03464	8,60911	351/154430	Turn from 351 to 301 pt 1
JC228_p351b	89,031	8,61218	351/154830	89,02293	8,65456	351/162900	Turn from 351 to 301 pt 2
JC228_p301	89,02548	8,65772	351/163203	89,25474	8,9325	351/210357	
JC228_p301a	89,256	8,93394	351/210530	89,20579	8,9797	351/222200	Turn from 301 to 302
JC228_p302	89,20506	8,97904	351/222246	88,97092	8,69832	352/032156	
JC228_p302a	88,96409	8,69041	352/032930	88,75258	8,54092	352/081000	Turn from 302 to 300
JC228_p300	88,75476	8,54339	352/081239	89,28379	9,17901	352/201705	
JC228_p303a	89,251	9,255	352/224630	89,14259	9,11809	353/010030	Part of 303 after gun maintenance
JC228_p303b	89,13164	9,10408	353/011430	89,10815	9,07491	353/014300	First part of 303 preplot
JC228_p303	89,14156	9,11667	353/010150	89,14076	9,11571	353/010250	Fragment due to Triggerfish crash
JC228_p303c	89,10409	9,06994	353/014754	88,86601	8,78481	353/062500	Second part of 303 preplot
JC228_p304	88,81665	8,83162	353/075433	89,04511	9,10539	353/125137	
JC228_p304a	89,04696	9,10764	353/125400	88,97303	9,13036	353/145330	Turn from 304 to 354 pt 1
JC228_p304c	88,9706	9,11863	353/150200	88,97944	9,09968	353/151630	Turn from 304 to 354 pt 2
JC228_p354	88,98224	9,09756	353/151854	89,26149	8,87016	353/194212	
JC228_p354a	89,2638	8,86815	353/194430	89,21773	8,81856	353/210230	Turn from 354 to 353
JC228_p353	89,21654	8,81953	353/210347	88,97935	9,02097	354/011530	End of shooting - medical emergency
JC228_p200_OBS_E	86,80296	10,7033	359/132900	88,50674	9,31449	360/175500	
JC228_p200b_MCS	88,54023	9,28695	361/132701	87,99258	9,74566	361/232812	MCS line from SW to grid 2
JC228_p200_c_MCS	87,94306	9,77435	361/232900	87,90228	9,76155	362/005500	Turn from p200b to 452
JC228_p452a	88,24376	9,44217	362/065600	88,19244	9,39793	362/083200	Turn from 452 to 451
JC228_p451	88,19052	9,39946	362/083355	87,91175	9,62583	362/130723	
JC228_p451a	87,90626	9,62895	362/131230	87,8913	9,55419	362/150830	Turn from 451 to 404
JC228_p404	87,92393	9,56576	362/153734	88,16973	9,85993	362/195514	
JC228_p404a	88,17184	9,86274	362/195730	88,22463	9,82026	362/212400	Turn from 404 to 403
JC228_p403	88,22425	9,81969	362/212439	87,80027	9,31284	363/075505	Includes extension outside main grid
JC228_p403a	87,79874	9,31064	363/075730	87,85467	9,27113	363/092630	Turn from 403 to 400
JC228_p400	87,85598	9,27264	363/092800	88,43447	9,96329	363/204631	
JC228_p400a	88,43612	9,96446	363/204800	88,47951	9,91368	363/220130	Turn from 400 to 402
JC228_p402	88,47845	9,91236	363/220254	88,27138	9,66359	364/021722	Includes extension outside main grid. End of shooting - guard boat distress call
JC228_p450	87,82124	9,9388	002/180000	87,93729	9,92061	002/192900	Mostly turn after deploy. streamer & guns
JC228_p450a	87,9416	9,92	002/193230	-88,04984	9,90226	002/210130	Diagonal to reach p455
JC228_p450b	88,06082	9,90066	002/211030	88,1265	9,88827	002/220300	Diagonal to reach p455
JC228_p455	88,12719	9,88779	002/220342	88,41585	9,65501	003/031531	
JC228_p455a	88,43574	9,6555	003/033130	88,45493	9,70652	003/042200	Turn to p402 part 1
JC228_p455b	88,44768	9,71234	003/042830	88,34544	9,75208	003/060330	Turn to p402 part 2
JC228_p402b	88,34492	9,75156	003/060407	88,06333	9,41489	003/122541	Southern part of p402
JC228_p402c	88,06077	9,41178	003/122900	88,11659	9,37271	003/140530	Turn from 402 to 401
JC228_p401	88,11719	9,37342	003/140614	88,32747	9,62465	003/181825	
JC228_p200d_MCS	88,55917	9,68769	003/224530	88,02503	9,70923	004/054200	Diagonal across grid 2 after reducing streamer
JC228_p200e_MCS	88,01913	9,71402	004/054716	87,04918	10,50254	004/213513	E part of p200 MCS, 3km streamer
JC228_p200f_MCS	87,04631	10,50388	004/213730	87,01009	10,44813	004/224030	Turn from p200 to 552
JC228_p552	87,01151	10,44693	004/224151	87,34159	10,1781	005/040421	
JC228_p552a	87,34411	10,17375	005/040830	87,29461	10,1299	005/051430	Turn from 552 to 551
JC228_p551	87,29281	10,13159	005/051613	86,97315	10,39049	005/102028	
JC228_p551a	86,97071	10,39265	005/102300	86,97769	10,2919	005/131730	Turn from 551 to 502
JC228_p502	86,97859	10,29279	005/131836	87,17262	10,52446	005/171001	
JC228_p502a	87,17428	10,52654	005/171200	-87,23255	10,4902	005/182400	Turn from 502 to 507
JC228_p507	87,23156	10,48886	005/182526	87,03748	10,25638	005/222148	

Tab. 7.4 Seismic profiles shot during JC228 leg 1

7.2 Station Lists of operations during leg 2

Station		Gear	Latitude		Longitude		Comment
COOK	SciParty		[°N]	[´N]	[°W]	[´W]	
JC228_hf01-01	HF2301P01	Heat flow/core barrel	10	14.7282	87	9.0666	successful
JC228_hf 01-02	HF2301P02	Heat flow/core barrel	10	14.9004	87	8.8500	successful
JC228_hf 01-03	HF2301P03	Heat flow/core barrel	10	15.0690	87	8.6395	successful
JC228_hf01-04	HF2301P04	Heat flow/core barrel	10	15.1590	87	8.5248	successful
JC228_hf01-05	HF2301P05	Heat flow/core barrel	10	15.2928	87	8.3700	successful
JC228_hf01-06	HF2301P06	Heat flow/core barrel	10	15.3960	87	8.2176	successful
JC228_hf01-07	HF2301P07	Heat flow/core barrel	10	15.5742	87	8.0286	successful
JC228_hf01-08	HF2301P08	Heat flow/core barrel	10	15.7242	87	7.8402	successful
JC228_hf02-01	HF2302P01	Heat flow/core barrel	10	17.602	87	12.010	successful
JC228_hf02-02	HF2302P02	Heat flow/core barrel	10	17.752	87	11.817	successful
JC228_hf02-03	HF2302P03	Heat flow/core barrel	10	17.920	87	11.610	successful
JC228_hf02-04	HF2302P04	Heat flow/core barrel	10	18.065	87	11.462	successful
JC228_hf02-05	HF2302P05	Heat flow/core barrel	10	18.246	87	11.220	successful
JC228_hf02-06	HF2302P06	Heat flow/core barrel	10	18.362	87	11.091	successful
JC228_hf02-07	HF2302P07	Heat flow/core barrel	10	18.461	87	10.950	successful
JC228_hf02-08	HF2302P08	Heat flow/core barrel	10	18.545	87	10.846	successful
JC228_hf02-09	HF2302P09	Heat flow/core barrel	10	18.692	87	10.693	successful
JC228_hf02-10	HF2302P10	Heat flow/core barrel	10	18.854	87	10.467	successful
JC228_hf03-01	HF2303P01	Heat flow/core barrel	10	14.815	87	21.949	successful
JC228_hf03-02	HF2303P02	Heat flow/core barrel	10	14.992	87	21.744	successful
JC228_hf03-03	HF2303P03	Heat flow/core barrel	10	15.164	87	21.526	successful
JC228_hf03-04	HF2303P04	Heat flow/core barrel	10	15.334	87	21.308	successful
JC228_hf03-05	HF2303P05	Heat flow/core barrel	10	15.514	87	21.098	successful
JC228_hf03-06	HF2303P06	Heat flow/core barrel	10	15.688	87	20.889	successful
JC228_hf03-07	HF2303P07	Heat flow/core barrel	10	15.856	87	20.678	successful
JC228_hf03-08	HF2303P08	Heat flow/core barrel	10	15.974	87	20.447	successful
JC228_hf03-09	HF2303P09	Heat flow/core barrel	10	16.182	87	20.248	successful
JC228_hf03-10	HF2303P10	Heat flow/core barrel	10	16.353	87	20.031	successful
JC228_hf04-01	HF2304P01	Heat flow/core barrel	10	24.108	87	20.045	successful
JC228_hf04-02	HF2304P02	Heat flow/core barrel	10	24.252	87	19.830	successful
JC228_hf04-03	HF2304P03	Heat flow/core barrel	10	24.452	87	19.624	successful
JC228_hf04-04	HF2304P04	Heat flow/core barrel	10	24.619	87	19.414	successful
JC228_hf04-05	HF2304P05	Heat flow/core barrel	10	24.792	87	19.205	successful
JC228_hf04-06	HF2304P06	Heat flow/core barrel	10	24.973	87	18.993	successful
JC228_hf04-07	HF2304P07	Heat flow/core barrel	10	25.170	87	18.743	successful
JC228_hf04-08	HF2304P08	Heat flow/core barrel	10	25.370	87	18.513	successful
JC228_hf04-09	HF2304P09	Heat flow/core barrel	10	25.482	87	18.363	successful
JC228_hf04-10	HF2304P10	Heat flow/core barrel	10	25.653	87	18.151	successful
JC228_hf05-01	HF2305P01	Heat flow/core barrel	09	46.968	86	40.583	successful
JC228_hf05-02	HF2305P02	Heat flow/core barrel	09	46.819	86	40.747	successful
JC228_hf05-03	HF2305P03	Heat flow/core barrel	09	46.680	86	40.920	successful
JC228_hf05-04	HF2305P04	Heat flow/core barrel	09	46.541	86	41.090	successful
JC228_hf05-05	HF2305P05	Heat flow/core barrel	09	46.380	86	41.249	successful
JC228_hf05-06	HF2305P06	Heat flow/core barrel	09	46.257	86	41.441	successful
JC228_hf05-07	HF2305P07	Heat flow/core barrel	09	46.123	86	41.602	successful
JC228_hf05-08	HF2305P08	Heat flow/core barrel	09	45.980	86	41.780	successful
JC228_hf05-09	HF2305P09	Heat flow/core barrel	09	45.835	86	41.944	successful
JC228_hf05-10	HF2305P10	Heat flow/core barrel	09	45.694	86	42.121	successful
JC228_hf05-11	HF2305P11	Heat flow/core barrel	09	45.547	86	42.293	successful
JC228_hf05-12	HF2305P12	Heat flow/core barrel	09	45.412	86	42.464	successful
JC228_hf06-01	HF2306P01	Heat flow/core barrel	10	9.118	87	19.639	successful
JC228_hf06-02	HF2306P02	Heat flow/core barrel	10	9.294	87	19.839	successful
JC228_hf06-03	HF2306P03	Heat flow/core barrel	10	9.499	87	20.061	No data
JC228_hf06-04	HF2306P04	Heat flow/core barrel	10	9.697	87	20.257	successful
JC228_hf06-05	HF2306P05	Heat flow/core barrel	10	9.897	87	20.488	No data
JC228_hf06-06	HF2306P06	Heat flow/core barrel	10	10.103	87	20.667	successful

Tab. 7.5.1 Heat flow sites of JC228 leg 2

Station		Gear	Latitude		Longitude		Comment
COOK	SciParty		[°N]	[´N]	[°W]	[´W]	
JC228_hf07-01	HF2307P01	Heat flow/core barrel	10	7.436	87	0.602	successful
JC228_hf07-02	HF2307P02	Heat flow/core barrel	10	7.578	87	0.396	successful
JC228_hf07-03	HF2307P03	Heat flow/core barrel	10	7.734	87	0.171	successful
JC228_hf07-04	HF2307P04	Heat flow/core barrel	10	7.880	86	59.956	successful
JC228_hf07-05	HF2307P05	Heat flow/core barrel	10	8.027	86	59.734	successful
JC228_hf07-06	HF2307P06	Heat flow/core barrel	10	8.192	86	59.526	successful
JC228_hf07-07	HF2307P07	Heat flow/core barrel	10	8.343	86	59.306	successful
JC228_hf07-08	HF2307P08	Heat flow/core barrel	10	8.495	86	59.099	successful
JC228_hf08-01	HF2308P01	Heat flow/core barrel	09	56.923	86	52.063	successful
JC228_hf09-01	HF2309P01	Heat flow/core barrel	09	51.115	86	47.387	successful

Tab. 7.5.2 Heat flow sites of JC228 leg 2, continued

Station No.	Date	Time	Latitude	Longitude	Water depth	Barrel Length	Core Recovered	Water samples taken
		[h]	[N°]	[W°]	[m]	[m]	[m]	
JC228B_GC_1	14.01.23	13:32	10.22031	87.29059	2966	9	4.83	21
JC228B_GC_2	15.01.23	13:44	10.26199	87.13075	3255	12	10.465	32
JC228B_GC_3	15.01.23	18:16	10.28838	87.15516	3249	12	6.26	22
JC228B_GC_4	16.01.23	17:51	10.30440	87.17937	3237	9	3.52	8
JC228B_GC_5	16.01.23	21:12	10.32075	87.19533	3151	6	5.09	11
JC228B_GC_6	16.01.23	23:46	10.34084	87.20328	2769	3	0	0
JC228B_GC_7	17.01.23	19:50	10.40739	87.28458	3220	6	6.065*	13
JC228B_GC_8	17.02.23	22:56	10.41566	87.30156	3153	9	2.35	5
JC228B_GC_9	18.01.23	20:00	10.36923	87.20912	1890	3	2.37	7
JC228B_GC_10	18.01.23	21:57	10.37276	87.21645	1908	3	0.25	0
JC228B_GC_11	19.01.23	18:57	9.770801	86.69054	3338	9	9.6#	19
JC228B_GC_12	20.01.23	13:50	10.16433 §	87.33992 §	2886	3	0.28	3
JC228B_GC_13	20.01.23	17:15	10.16483 §	87.34141 §	2895	3	0	0
JC228B_GC_14	21.01.23	10:22	10.13982 §	86.98971 §	3339	9	8.305	17
JC228B_GC_15	21.01.23	16:00	9.94869 §	86.86773 §	3278	9	5.15	11
JC228B_GC_16	21.01.23	19:45	9.85192 §	86.78979 §	3347	9	8.56*	16

Date and Time are UTC,
latitude and longitude are from the USBL mounted on the corer, recorded when the corer was on the seabed
* includes material extracted from bomb as over-penetrated.
# over-penetrated in to bomb, possibly some lost in upper ~1.5m during extraction.
§ USBL beacon located on wire 50m above corer

Tab. 7.6 Sediment coring sites

8 Data and Sample Storage and Availability

Seismic refraction data will be available after 1st of February 2025 at the PANGAEA World Data Centre, Bremerhaven (http:// http://www.pangaea.de) and the British Oceanographic Data Centre or BODC (www.bodc.ac.uk/), multichannel seismic, gravity and magnetic data from the BODC.

Bathymetric data recorded during the survey will be archived both at PANGAEA and BODC.

Table 8.1 Overview of data availability

Type	Database	Available	Free Access	Contact
EM122	PANGAEA, BODC	1.5.2023	1.2.2025	igrevemeye@geomar.de; iklaucke@geomar.de T.J.Henstock@soton.ac.uk
OBS data	PANGAEA,	1.5.2023	1.2.2025	igrevemeyer@geomar.de
OBIC OBS data	BODC	1.7.2023	1.2.2025	T.J.Henstock@soton.ac.uk
Gravity	BODC	1.7.2023	1.2.2025	T.J.Henstock@soton.ac.uk
Magnetic data	BODC	1.7.2023	1.2.2025	T.J.Henstock@soton.ac.uk
Pore water	BODC	1.7.2024	1.2.2025	matthew.cooper@noc.soton.ac.uk Damon.Teagle@southampton.ac.uk
Heat Flow	PANGAEA	1.5.2023	1.2.2025	nkaul@uni-bremen.de

PANGAEA: World Data Centre, Bremerhaven (htwww.pangaea.de)
BODC: British Oceanographic Data Centre (www.bodc.ac.uk/)

9 Acknowledgements

We acknowledge the excellent and professional sea-going operation of RRS JAMES COOK during JC228 by Captain John Leask and his crew. This was a barter cruise conducted under the umbrella of the European *Ocean Facility Exchange Group* (OFEG), which was funded by the German Ministry of Education, Science and Research (BMBF) though grant 03G0295OA to GEOMAR and UK's Natural Environment Research Council (NERC) under grant NE/M021246/1 to University of Southampton. The wide-angle seismic data were recorded with instruments provided by and GEOMAR as well as NERC's Ocean-Bottom Instrumentation Facility. The seismic streamer, airguns, gravimeter, magnetometer, the AUV AutoSUB as well as the coring device was provided and run by the NERC's National Marine Equipment Facility, together with installation and technical support during the marine operations. The seismic streamer was provided by (hired from) the Spanish Consejo Superior de Investigaciones Científicas (CSIC). Heat flow measurements were funded by BMBF grant 03G0295OB to the University of Bremen.

10 References

Aghaei, O., Nedimovic, M.R., Carton, H., Canales, J.P., Carbotte, S.M. & Mutter, J.C., 2014. Crustal thickness andMoho character from poststackmigrated 3D MCS data collected over the fast-spreading East Pacific Rise from 9º42 N to 9º57’N, Geochem. Geophys. Geosyst., 15, 634–657.

Barth, G.A., and J.C. Mutter, 1996. Variability in oceanic crustal thickness and structure: Multichannel seismic reflection results from the northern East Pacific Rise, J. Geophys. Res., 101, 17,951–17,975, https://doi.org/10.1029/96JB00814.

Canales, J. P., R. S. Detrick, S. Bazin, A. J. Harding and J. A. Orcutt, 1998. Off-axis crustal thickness variations across and along the East Pacific Rise within the MELT area, Science, 280, 1218-1221.

Contreras-Reyes, E., I. Grevemeyer, E.R. Flueh, C. Reichert, 2008, Upper lithospheric structure of the subduction zone offshore of southern Arauco Peninsula, Chile at ~38° S, J. Geophys. Res., 113, B07303, doi:10.1029/2007JB005569.

Contreras-Reyes, E., I. Grevemeyer, A. B. Watts, E. R. Flueh, C. Peirce, S. Moeller, and C. Papenberg, 2011, Deep seismic structure of the Tonga subduction zone: Implications for mantle hydration, tectonic erosion, and arc magmatism, J. Geophys. Res., 116, doi:10.1029/2011JB008434

Davis, E.E., and H. Villinger, 1992. Tectonic and thermal structure of the middle valley sedimented rift, northern Juan de Fuca Ridge. Proc. ODP Initial Rep., 139, 9-41.

Detrick, R. S., P. Buhl, E. Vera, J. Mutter, J. Orcutt, J. Madsen, and T. Brocher, 1987, Multi-channel seismic imaging of an axial magma chamber along the East Pacific Rise between 9°N and 13°N, Nature, 326, 35–41.

Dilek, Y. 2003, Ophiolite concept and its evolution, GSA Special Paper 373, 1-16.

Fisher, A.T., K. Becker, and T.N. Narasinham, 1994. Off-axis hydrothermal circulation: Parametric test of a refined model of processes at DSDP/ODP site 504. J. Geophys. Res., 99: 3097-3121.

Grevemeyer, I. and A. Bartetzko, 2003. Hydrothermal ageing of oceanic crust: inferences from seismic studies and well logging, in Hydrogeology of Oceanic Lithosphere, eds. E.E. Davis and H. Elderfield, Cambridge University Press., pp 128-150.

Grevemeyer, I., W. Weigel, and C. Jennrich, 1998. Structure and ageing of oceanic crust at 14°S on the East Pacific Rise, Geophys. J. Int., 135: 573-584.

Grevemeyer, I., N. Kaul, H. Villinger, and W. Weigel, 1999. Hydrothermal activity and the evolution of the seismic properties of upper oceanic crust, J. Geophys. Res., 104: 5069-5079.

Grevemeyer, I., N. Kaul, J.L. Diaz-Naveas, H. Villinger, C.R. Ranero, C. Reichert, 2005, Heat flow and bending-related faulting at subduction trenches: case studies offshore of Nicaragua and Central Chile, Earth Planet. Sci. Lett., 236, 238-248.

Grevemeyer, I., C.R. Ranero, E.R. Flueh, D. Klaeschen, J. Bialas, 2007, Passive and active seismological study of bending-related faulting and mantle serpentinization at the Middle America trench. Earth Planet. Sci. Lett., 258, 528-542

Grevemeyer, I., C. R. Ranero, and M. Ivandic, 2018, Structure of oceanic crust and serpentinization at subduction trenches. Geosphere, 14(2), 395–418. https://doi.org/10.1130/GES01537.1

Heesemann, M., I. Grevemeyer, H. Villinger, 2009, Thermal constraints on the frictional conditions of the nucleation and rupture area of the 1992 Nicaragua tsunami earthquake, Geophys. J. Int., 1265-1278, doi:10.1111/j.1365-246X.2009.04187.x

Houtz, R., and J. Ewing, 1976. Upper crustal structure as a function of plate age. J. Geophys. Res., 81: 2490-2498.

Hutnak, M., A. T. Fisher, R. Harris, C. Stein, K. Wang, G. Spinelli, M. Schindler, H. Villinger, and E. Silver, 2008. Surprisingly large heat and fluid fluxes driven through midplate outcrops on ocean crust, Nat. Geosci., 1, 611–614, doi:10.1038/ngeo264.

Hyndman, R.D., and M.J. Drury, 1976. The physical properties of oceanic basement rocks from deep drilling on the Mid-Atlantic Ridge. J. Geophys. Res., 81, 4042-4060.

Ildefonse, B., et al., 2010, The MoHole: A Crustal Journey and Mantle Quest, Workshop in Kanazawa, Japan, 3–5 June 2010. Scientific Drilling, 10, 56-62.

Ivandic, M., I. Grevemeyer, J. Berhorst, E.R. Flueh, K. McIntosh, 2008, Impact of bending related faulting on the seismic properties of the incoming oceanic plate offshore of Nicaragua, J. Geophys. Res., 133, B05410, doi:10.1029/2007JB005291

Kodeira, K., G. Fujie, M. Yamashita, T. Sato, T. Takahashi, N., Takahashi, 2014, Seismolgical evidence of mantle floe driving plate motons at a palaeo-spreading centre, Nature Geosciences, 7, 371–375.

Korenaga, J., W. S. Holbrook, G. M. Kent, P. B. Kelemen, R. S. Detrick, H.-C. Larsen, J. R. Hopper, and T. Dahl-Jensen, 2000, Crustal structure of the southeast Greenland margin from joint refraction and reflection seismic tomography, J. Geophys. Res., 105(B9), 21, 591–21, 614, doi:10.1029/2000JB900188.

Korenaga, J., P. B. Kelemen, and W. S. Holbrook, 2002. Methods of resolving the origin of large igneous provinces from crustal seismology, J. Geophys. Res., 107, 2178, doi:10.1029/2001JB001030.

Langseth, M.G., P.J. Grim, and M. Ewing, 1965. Heat flow measurements in the East Pacific Ocean, J. Geophys. Res., 70: 367-380.

Lefeldt, M., I. Grevemeyer, J. Goßler, J. Bialas, 2009, Intraplate seismicity and related mantle hydration at the Nicaraguan trench-outer rise, Geophys. J. Int., 178, 742-752, doi:10.1111/j.1365-246X.2009.04167.x

Lister, C.R.B., 1972. On the thermal balance of a mid-ocean ridge. Geophys. J. R. Astron. Soc., 26: 515-535.

Lister, C.R.B., 1979. The pulse-probe method of conductivity measurement. Geophys. J. R. Astr. Soc. 57, 451–461.

Marjanović, M., H. D. Carton, M. R. Nedimović, S. M. Carbotte, J. Mutter, J. P. Canales, 2015, Distribution of melt along the East Pacific Rise from 9º30′ to 10ºN from an amplitude variation with angle of incidence (AVA) technique, Geophysical Journal International 203, 1-21; doi: 10.1093/gji/ggv251

Marjanović., M., S.M., Carbotte, H, Carton, M.R., Nedimović, J.P., Canales, & J.C., Mutter 2018, Crustal Magmatic System Beneath the East Pacific Rise (8º20′ to 10º10′ N):

Implications for Tectono-magmatic Segmentation and Melt Transport at Fast-spreading Ridges, Geochemistry, Geophysics, Geosystems, 10.1029/2018GC007590.

McKenzie, D. P., and M. J. Bickle, 1988. The volume and composition of melt generated by extension of the lithosphere, J. Petrol., 29, 625–679.

Müller, R.D., Sdrolias, M., Gaina, C., and Roest, W. R., 2008. Age, spreading rates, and spreading asymmetry of the world's ocean crust, Geochem. Geophys. Geosyst., 9, Q04006, doi:10.1029/2007GC001743.

Raitt, R.W., 1963. The crustal rocks, in The sea, Vol. 3, ed. M.N. Hill, Interscience, New York, 85-102.

Reston, T. J., Ranero, C. R., Belykh, I. 1999, The structure of Cretaceous oceanic crust of the NW Pacific: Constraints on processes at fast spreading centres. J. Geophys. Res. 104, 629-644.

Stein, C.A., S. Stein, 1994. Constraints on hydrothermal heat flux trough the oceanic lithosphere from global heat flow. J. Geophys. Res., 99: 3081-3095.

Teagle, D.,A.H., Ildefonse, B., 2011. Journey to the Mantle of the Earth, Nature, 471, 437-439.

Teagle, D.A, et al., 2012, IODP Expedition 335: Deep Sampling in ODP Hole 1256D, Scientific Drilling, 13, 28-34.

Umori, S., et al., 2012, MOHOLE TO THE MANTLE (M2M), IODP-proposal 805-MDP

Villinger, H., Davis, E. E., 1987, A New Reduction Algorithm for Marine Heat Flow Measurements. Journal of Geophysical Research 92 (B12), 12846–12856.

Villinger, H., I. Grevemeyer, N. Kaul, J. Hauschild, and M. Pfender, 2002. Hydrothermal heat flux through aged oceanic crust: where does the heat escape?. Earth Planet. Sci. Lett., 202: 159-170.

Villinger, H. W., T. Pichler, N. Kaul, S. Stephan, H. Palike, and F. Stephan, 2017, Formation of hydrothermal pits and the role of seamounts in the Guatemala Basin (Equatorial East Pacific) from heat flow, seismic, and core studies, Geochem. Geophys. Geosyst., 18, 369–383, doi:10.1002/2016GC006665.

White, R.S., D. McKenzie, and R.K. O'Nions, 1992. Oceanic crustal thickness from seismic measurements and rare earth element inversion. J. Geophys. Res., 97: 19683-19715.

Whitmarsh, R.B., 1978. Seismic refraction studies of the upper igneous crust in the North Atlantic and porosity estimates for layer 2. Earth Plant. Sci. Lett., 37: 451-464.

Wilson, D.S., 1996. Fastest known spreading on the Miocene Cocos-Pacific plate boundary. Geophys. Res. Lett., 23:3003–3006. doi:10.1029/96GL02893

Wilson, D.S., Hallenborg, E., Harding, A.J., and Kent, G.M., 2003. Data report: Site survey results from cruise EW9903. In Wilson, D.S., Teagle, D.A.H., Acton, G.D., Proc. ODP, Init. Repts., 206, 1–49, Texas A&M University, College Station TX 77845-9547, USA.

11 Abbreviations

OBS – Ocean-Bottom-Seismometer

MMO – Marine Mammal Observation

HF – Heat flow

AUV – Autonomous Underwater Vehicle

12 Appendices

12.1 Selected Pictures of Shipboard Operations